International Journal of Fracture manuscript No.
(will be inserted by the editor)

Tough-brittle transition in unidirectional composites with fibre breakage and fibre-matrix interfacial failure

Sivasambu Mahesh

Received: date / Accepted: date

Abstract Fracture of three-dimensional unidirectional composites is studied through Monte Carlo fracture simulations on model composites. Fracture develops in the model composites by the failure of fibre segments wherein the tensile stress exceeds a Weibull-distributed random strength, and by the failure of the fibre-matrix interfaces wherein the shear stress exceeds a deterministic interfacial strength, T_0. The size of the weakest-link failure event is inferred from empirical strength distributions obtained from the simulations. It is found to diverge or converge with composite size for T_0 below or above a threshold value, respectively. The threshold is identified as the tough-brittle fracture mode transition. The mechanistic cause underlying the transition is also identified.

Keywords Polymer matrix composite, Fracture mode transition, Random strength, Probability distribution

Sivasambu Mahesh

Department of Aerospace Engineering, Indian Institute of Technology Madras, Chennai 600036, India.

E-mail: smahesh@iitm.ac.in

1 Introduction

1.1 The fibre-matrix interface

The fracture surface of unidirectional polymer matrix fibre composites subjected to longitudinal uniaxial tension can be smooth, step-like, broom-like, or brush-like (Hull and Clyne 1996; Robinson et al 2012). The nature of the fracture surface is determined by the shear strength of the fibre-matrix interface relative to the tensile strength of the fibres (Hull and Clyne 1996, Chap. 8). A strong interface results in brittle fracture with a smooth fracture surface (Hull and Clyne 1996, Fig. 8.10), while a weak interface is associated with a brush-like fracture surface (Hull and Clyne 1996, Fig. 8.8). Intermediate interfacial strengths result in random variability in the nature of the fracture surface. For example, Ma et al (2016, 2017) observed fracture surface variation from step-like to brush-like amongst nominally identical specimen. They attributed this variation to fluctuations in the local interfacial strength.

The fibre-matrix interface derives its strength from two physical mechanisms: adhesion, or chemical bonding between the fibre and matrix, and friction (Zhandarov and Mäder 2005). The strength imparted by these mechanisms depends on the fibre and matrix materials (Herrera-Franco and Drzal 1992), and on the methods adopted for interphase tailoring (Karger-Kocsis et al 2015). Banholzer and Brameshuber (2001) have proposed a phenomenological multilinear model of the interfacial shear stress variation with interfacial slip, incorporating these mechanisms. Their model is summarised in Fig. 1. In this model, the fibre-matrix interface is assumed chemically adhered (bonded) in region I. The relative displacement between fibre and matrix in this region accrues from their elastic deformation. Region II describes the regime of an imperfectly bonded interface, and region III, a completely debonded interface with relative motion across the interface, and frictional forces on such fibre and matrix segments.

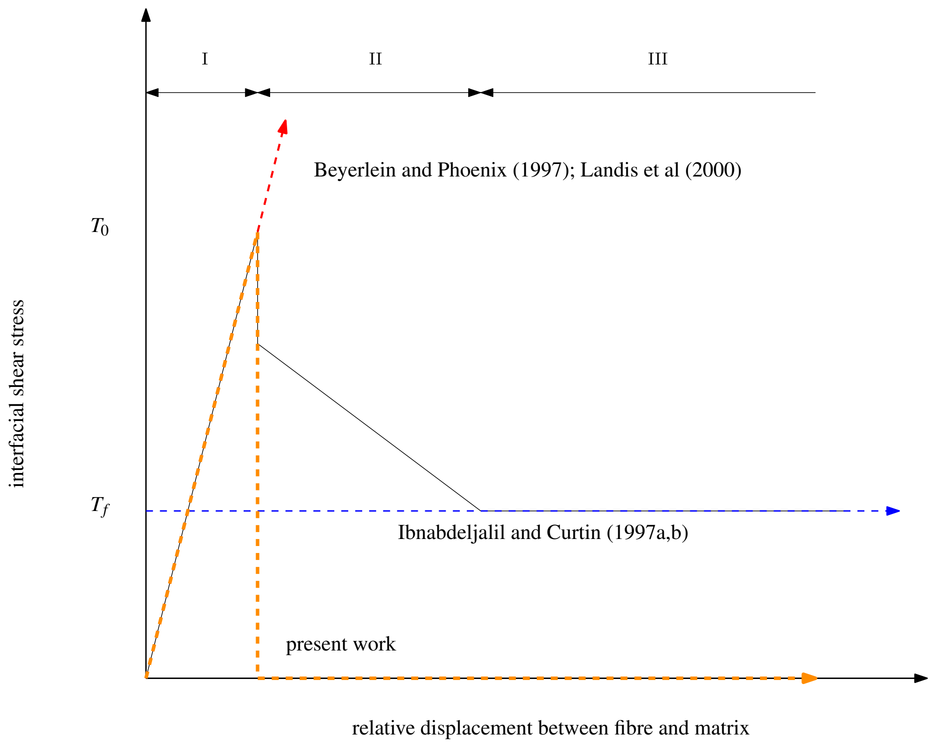

Fig. 1: Schematic of the multilinear interfacial response model due to Banholzer and Brameshuber (2001) is depicted by the solid black line. T_0, and T_f are the interfacial strength, and interfacial frictional stress, respectively. Idealised interfacial response assumed by Beyerlein and Phoenix (1997), Landis et al (2000), Ibnabdeljalil and Curtin (1997a,b), and the present work are indicated by broken lines.

1.2 Composite strength distribution

In a polymer matrix unidirectional composite loaded in tension along the fibre direction, the stiff fibres carry almost the entire the applied load (Hull and Clyne 1996). Fibre strengths, governed by the presence of flaws, are randomly distributed (Hull and Clyne 1996). The ultimate tensile strength depends not only on the strength distribution of the fibres, but also on the load redistribution from broken fibres to intact ones. Load redistribution, in turn, depends on the matrix material properties, and on the characteristics of the fibre-matrix interface.

Monte Carlo simulation studies of fracture development in polymer matrix composites in the literature have generally assumed a perfectly bonded interface. Fig. 1 places this assumption in the context of the Banholzer and Brameshuber (2001) model. Beyerlein and Phoenix (1997) and Landis et al (2000) studied the fracture of two- and three-dimensional model composites respectively, through Monte Carlo fracture simulations. They implemented a localised load transfer model, i.e., one which overloads nearby intact neighbours of a broken fibre severely, relative to more distant neighbours. They found that model composites undergo brittle fracture by the nucleation of a critical cluster of fibre breaks, followed by its propagation. They showed that this failure mode results in the composite strength distribution obeying weakest-link scaling.

To the author's knowledge, a failing interface has not been accounted for in simulation studies of polymer matrix composites. However, the influence on composite strength of a debonded frictionally sliding interface, which is realised in ceramic matrix composites has been well-studied (Ibnabdeljalil and Curtin 1997a,b). The idealised frictional interfacial response is also sketched in Fig. 1. In three-dimensional model specimen, Ibnabdeljalil and Curtin (1997a) showed that weakest-link scaling is observed, provided load transfer from broken to intact fibres the fibre breaks is highly localised. Also, under the same load transfer conditions, Ibnabdeljalil and Curtin (1997b) showed that the strength of notched fibre composites can be explained by weakest-link failure considerations.

1.3 Fracture mode transition

On the one hand, the works described in Sec. 1.2 indicate that a strong interface results in localised load sharing, which in turn results in a brittle fracture mode. On the other hand, if the interfacial strength were negligible, the fibre-matrix interface will fail at each fibre break, and the interfacial crack will propagate along the fibre direction indefinitely. Such a composite will behave like a loose bundle of threads, wherein the load dropped by the broken fibre is distributed equally amongst the intact ones. Fracture develops in a loose bundle by spatially uncorrelated fibre breakage, giving it a tough characteristic (Hansen et al 2015). In between, there may exist an intermediate value of interfacial shear strength at which the failure mode transitions from brittle to tough. Experimentally also, the existence of the tough-brittle transition in polymer matrix composites is suggested by the very different modes of fracture development in carbon and glass fibre reinforced polymer matrix composites, the former characterised by a strong interface, and the latter by a weak one (Scott et al 2011; Sket et al 2012; Kumar et al 2012).

1.4 Present work

In the present work, the fibre-matrix interface in the model polymer matrix composite is endowed with a finite shear strength, T_0. It remains perfectly bounded as long as the interfacial shear stress is less than T_0 during composite loading. When the interfacial shear stress equals T_0, the interface is taken to fail. Thereafter, the interface transmits no shear. Thus, shear stress transmitted by a debonded interface due to friction is neglected. The assumed interfacial characteristic is shown schematically in Fig. 1.

Monte Carlo simulations of three-dimensional polymer matrix composite fracture are performed for various interfacial shear strengths, with the particular aim of identifying the transitional value of T_0, and the qualitative differences in fracture development in the brittle and tough regimes. These simulations are enabled by a recently developed fast computational framework (Mahesh 2020) for performing stress analyses in a simulation cell with elastically interacting, arbitrarily distributed fibre breaks, and fibre-matrix interface failures.

In order to directly capture the fracture mode transition in physically-sized composites, fracture in similarly sized computer models must be simulated. However, computational complexity limits the simulations to much smaller sizes. Therefore, presently, the size of the weakest-link failure event is estimated for various system sizes, and its scaling with system size is used to extrapolate to large system sizes. This methodology extends the approach developed by Kachhwah and Mahesh (2020).

2 Model composites

2.1 Three-dimensional model composite

The three-dimensional (3D) model composite is comprised of ν^2 unidirectional fibers arranged in a hexagonal lattice, as shown in Fig. 2. Its cross-section is rhombus-shaped. Fibres are assumed to be cylindrical with cross-sectional area A, and linear elastic with Youngs modulus E. The centre-to-centre distance between adjacent fibres is denoted d. The model composite is loaded in tension along the fibre direction. Fibres are assumed to be much stiffer in the longitudinal direction than the matrix, and thus carry almost all the tensile load. The matrix material is assumed to be loaded predominantly in shear. The shear stiffness of the matrix is denoted Gh, where G is the matrix shear modulus, and h is comparable to the fibre diameter.

The transverse distance between fibres is normalised by d, so that the normalised centre-to-centre distance between a pair of neighbouring fibres is unity. The normalised position

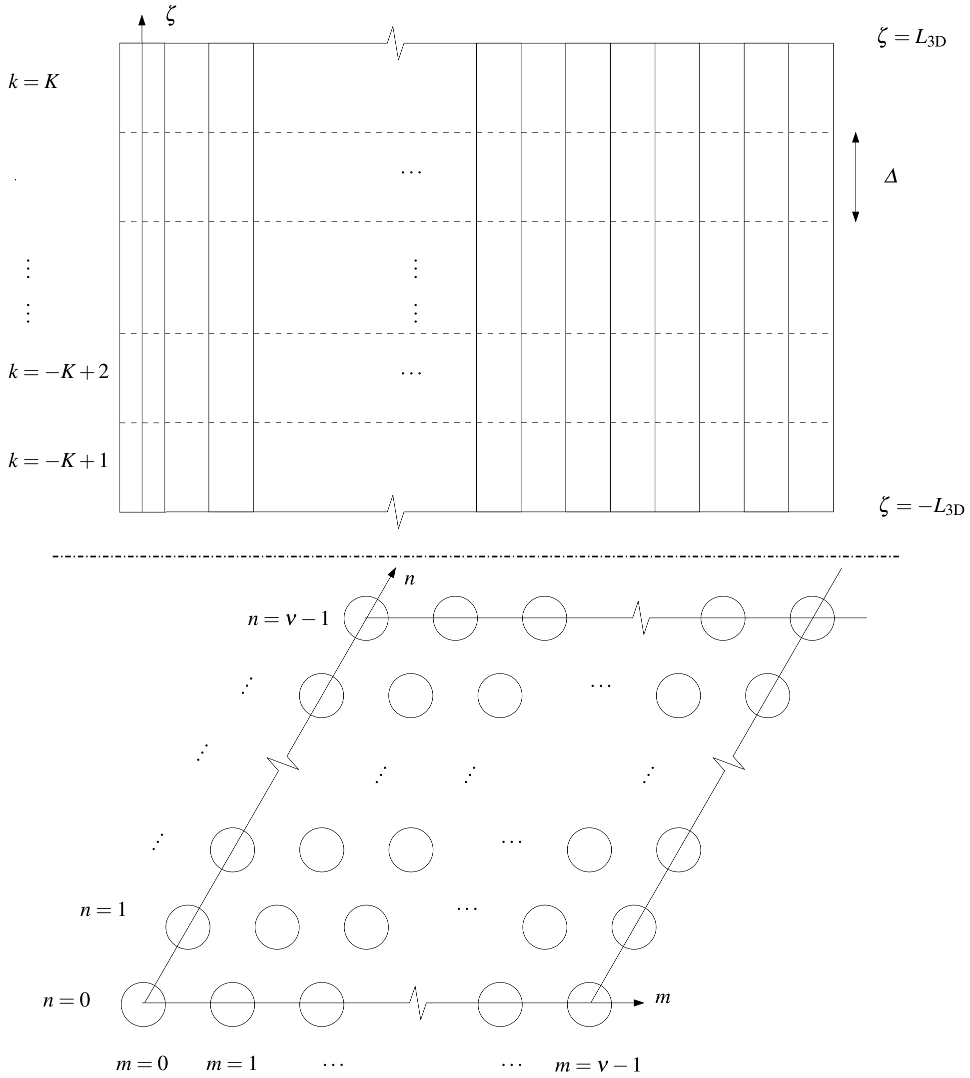

Fig. 2: The 3D periodic model composite comprised of $\nu \times \nu$ fibres of length $2L_{3D}$ arranged in a hexagonal lattice. The m–n–ζ coordinate system is shown. The model is longitudinally divided into $2K$ blocks, each of length $\Delta = L_{3D}/K$. Fibre breaks are restricted to the block boundaries, at $\zeta = k\Delta$, $k \in \{-K+1, -K+2, \ldots, K\}$. Matrix failures extend one or more blocks, and occur due to debonding at the fibre-matrix interface.

of a fibre is specified with respect to the non-orthogonal (m,n) coordinate system shown in Fig. 2. Also, the distance along the fibre direction, z, is non-dimensionalised as

$$\zeta := z\sqrt{\frac{Gh}{EAd}}, \tag{1}$$

following Hedgepeth (1961), and Hedgepeth and Van Dyke (1967). The finite 3D model composite is taken to extend over $z \in [-\ell_{3D}, \ell_{3D}]$. Letting $L_{3D} = \ell_{3D}\sqrt{Gh/(EAd)}$, the non-dimensional longitudinal extent is $\zeta \in [-L_{3D}, L_{3D}]$, according to Eq. (1). It is divided into $2K$ blocks, each of normalised length

$$\Delta := L_{3D}/K, \tag{2}$$

as shown in Fig. 2. The k-th block, $k \in \{-K+1, -K+2, \ldots, K\}$ extends over $\zeta \in (k\Delta, (k+1)\Delta)$.

Periodicity is assumed along the m, n, and ζ axes. Thus, the fibres $(m=0,n)$ abut $(m=\nu-1,n)$, for all $n \in \{0,1,\ldots,\nu-1\}$ and fibres $(m,n=0)$ abut $(m,n=\nu-1)$, for all $m \in \{0,1,\ldots,\nu-1\}$. Also, along the ζ direction, the transverse sections $\zeta = \pm L_{3D}$ coincide. Because of the longitudinal and transverse periodicity, fibre coordinates (m,n), and block indices k are only significant modulo ν, and $2K$, respectively. These are denoted $[m]$, $[n]$, and $[k]$, and defined as

$$\begin{aligned} [m] &:= m - \nu\lfloor m/\nu \rfloor, \\ [n] &:= n - \nu\lfloor n/\nu \rfloor, \text{ and} \\ [k] &:= k - 2K\lfloor (k+K-1)/(2K) \rfloor, \end{aligned} \tag{3}$$

where $\lfloor\cdot\rfloor$ denotes the largest integer no greater than its argument.

Let $v_{mn}(z)$ be the fibrewise displacement in fibre (m,n) at z. The stress at that point is given by $E dv_{mn}/dz$. The average fibre stress at cross-section z is given by

$$\langle\sigma\rangle = \frac{E}{\nu^2}\sum_{m=0}^{\nu-1}\sum_{n=0}^{\nu-1}\frac{dv_{mn}}{dz}(z). \tag{4}$$

Equilibrium demands that $\langle\sigma\rangle$ be independent of z. Following Hedgepeth (1961, Eq. 6), the non-dimensional fibre displacement is defined as

$$u_{mn} = v_{mn}\sqrt{\frac{EGh}{Ad}}\frac{1}{\langle\sigma\rangle}. \tag{5}$$

Eqs. (1), and (5) together imply

$$\frac{du_{mn}}{d\zeta} = \frac{E}{\langle\sigma\rangle}\frac{dv_{mn}}{dz}. \tag{6}$$

The non-dimensional stress associated with u_{mn}, σ_{mn} physically represents the stress concentration, and is defined as

$$\sigma_{mn}(\zeta) := \frac{du_{mn}}{d\zeta}(\zeta). \tag{7}$$

The stress overload is defined as the stress concentration less unity:

$$\tilde{\sigma}_{mn}(\zeta) := \sigma_{mn}(\zeta) - 1. \tag{8}$$

The longitudinal division of the composite into $2K$ blocks divides each fibre into segments of length Δ. The k-th segment in fibre (m,n) extends $\Delta/2$ either side of $\zeta = k\Delta$, i.e., over $\zeta \in (([k-1]+1/2)\Delta, k\Delta) \cup (k\Delta, ([k+1]-1/2)\Delta)$. It is assigned a random strength, Σ^{3D}_{mnk}, drawn from the Weibull (1952) distribution:

$$F_{3D}(\sigma) = \Pr\{\Sigma^{3D}_{mnk} \le \sigma\} = 1 - \exp\left(-\Delta\left(\frac{\sigma}{\sigma_0}\right)^{\rho}\right). \tag{9}$$

Here, ρ is called the Weibull exponent, and σ_0 is called the scale factor. Variability of fibre segment strength increases with decreasing ρ. Physically, a fibre segment may break anywhere along its length. However, presently, for reasons of computational efficiency, the fibre breaks are restricted to the mid-point of the fibre segment, $\zeta = k\Delta$. The consequences of this assumption are examined in Sec. 4.

The k-th segment in fibre (m,n) is identified by the indices mnk. The stress concentration, and stress overload at the potential site of fibre breakage are denoted

$$\begin{aligned}\sigma_{mnk} &:= \sigma_{mn}(\zeta = k\Delta), \text{ and} \\ \tilde{\sigma}_{mnk} &:= \tilde{\sigma}_{mn}(\zeta = k\Delta),\end{aligned} \tag{10}$$

respectively. The fibre segment mnk is assumed to fail if

$$\Sigma^{\text{3D}}_{mnk} \leq \sigma_{mnk}\langle\sigma\rangle. \tag{11}$$

Matrix bays between adjacent fibres (m,n), and $([m+1],n)$; (m,n), and $(m,[n+1])$; and (m,n), and $([m-1],[n+1])$, are identified by the indices mni, for $i=1$, 2, and 3, respectively. Following Hedgepeth (1961), the shear flow in the matrix bay mni is defined as

$$T_{mni} = \frac{Gh}{d} \times \begin{cases} (v_{[m+1],n} - v_{mn}), & \text{if } i=1, \\ (v_{m,[n+1]} - v_{mn}), & \text{if } i=2, \\ (v_{[m-1],[n+1]} - v_{mn}), & \text{if } i=3. \end{cases} \tag{12}$$

The segment of matrix bay mni contained in the k-th block is identified by the indices $mnik$. Matrix bay segment $mnik$ is taken to fail if the fibre-matrix interface with either of its flanking fibres debonds. Debonding is taken to occur if the maximum of the magnitude of the shear flow, T_{mni}, over block k, exceeds a deterministic shear strength, T_0. Since fibre breaks are restricted to the ends of the blocks, the maximum is realised at one of the ends of block k. Thus,

$$T_{mnik} := \max\left(|T_{mni}(\zeta = k\Delta)|, |T_{mni}(\zeta = [k+1]\Delta)|\right), \tag{13}$$

and the criterion for the failure of matrix segment, $mnik$, is

$$T_0 \leq T_{mnik}\langle\sigma\rangle. \tag{14}$$

Let the shear flow T_{mni} be non-dimensionalised as

$$T_{mni} = \sqrt{\frac{GAh}{Ed}} \langle\sigma\rangle \tau_{mni}, \tag{15}$$

so that

$$\tau_{mni}(\zeta) = \begin{cases} u_{[m+1],n}(\zeta) - u_{mn}(\zeta), & \text{if } i = 1, \\ u_{m,[n+1]}(\zeta) - u_{mn}(\zeta), & \text{if } i = 2, \\ u_{[m-1],[n+1]}(\zeta) - u_{mn}(\zeta), & \text{if } i = 3, \end{cases} \tag{16}$$

and

$$\tau_{mnik} := \max\left(|\tau_{mni}(\zeta = k\Delta)|, |\tau_{mni}(\zeta = [k+1]\Delta)|\right). \tag{17}$$

In terms of τ_{mnik}, Eq. (14), the condition for the failure of matrix bay segment, *mnik*, becomes

$$\tau_0 \leq \tau_{mnik} \langle\sigma\rangle, \tag{18}$$

where, $\tau_0 = T_0\sqrt{Ed/(GAh)}$. It emphasised that matrix bay segment *mnik* must either be failed, or intact. Partial failure is not permitted in order to gain computation speed.

The average longitudinal strain in the fibres is given by

$$\begin{aligned} \langle\varepsilon\rangle &= \frac{(v_{mn}(z = \ell_{3\text{D}}) - v_{mn}(z = -\ell_{3\text{D}}))}{2\ell_{3\text{D}}} \\ &= \frac{\langle\sigma\rangle}{E} \frac{(u_{mn}(\zeta = L_{3\text{D}}) - u_{mn}(\zeta = -L_{3\text{D}}))}{2L_{3\text{D}}}. \end{aligned} \tag{19}$$

The second expression follows from the normalising Eqs. (1), and (5). The normalised average longitudinal strain is defined as

$$\langle\bar{\varepsilon}\rangle = \frac{E}{\sigma_0} \langle\varepsilon\rangle \tag{20}$$

2.2 Fracture simulation in 3D composites

Monte Carlo fracture simulations are performed on N_{sim} realisations of statistically identical specimen. Each simulation begins by assigning random strengths $\Sigma_{mnk}^{3\mathrm{D}}$ to the $2K\nu^2$ fibre segments drawn from Eq. (9). The form of Eq. (9) also suggests $\langle\sigma\rangle/\sigma_0$ as a convenient loading parameter. Model specimens are loaded by monotonically increasing this parameter. Also, the failure criteria for fibres, and matrix bays, Eqs. (11), and (18), can be written in terms of the loading parameter as

$$\frac{\Sigma_{mnk}^{3\mathrm{D}}}{\sigma_0} \leq \sigma_{mnk} \frac{\langle\sigma\rangle}{\sigma_0}, \tag{21}$$

and

$$\frac{\tau_0}{\sigma_0} \leq \tau_{mnik} \frac{\langle\sigma\rangle}{\sigma_0}, \tag{22}$$

respectively.

In the first step, $\langle\sigma\rangle/\sigma_0$ is incremented so that the weakest fibre segment fails. The stress concentration in all the fibre segments, σ_{mnk}, and normalised shear stress in all the matrix bays, τ_{mnik} is calculated. This is the most computationally intensive step of the simulation, and is done using the fast Fourier transform based algorithm given by Mahesh (2020). If any more fibre breaks or matrix failures occur, following the criteria in Eq. (11), and (22), respectively, the corresponding elements are failed. The process of recomputing the stress concentrations, and failing fibre and matrix bay segments at the same $\langle\sigma\rangle/\sigma_0$ is continued until no more elements fail. At this point, $\langle\sigma\rangle/\sigma_0$ is incremented so that exactly one additional fibre or matrix bay segment fails. Additional failures at the same stress level, induced by stress concentrations are also generated, as described above.

The process of incrementing $\langle\sigma\rangle/\sigma_0$, and determining the set of failed elements is continued until a crack that traverses the specimen forms. The crack may be comprised of fibre breaks, and matrix failures, and will typically not be confined to a single transverse plane. A graph-based algorithm to detect the formation of the contiguous crack was given by Mahesh (2020).

The value of $\langle\sigma\rangle$ at which the model specimen i fractures is its ultimate strength, and is denoted $\langle\sigma\rangle_i^{\mathrm{ult}}$, for $i \in \{1,2,\ldots,N_{\mathrm{sim}}\}$. Let the ultimate strengths be sorted in ascending order, $\langle\sigma\rangle_{(1)}^{\mathrm{ult}} \leq \langle\sigma\rangle_{(2)}^{\mathrm{ult}} \leq \ldots \leq \langle\sigma\rangle_{(N_{\mathrm{sim}})}^{\mathrm{ult}}$. Then, the empirical 3D strength distribution is defined as:

$$H_{3\mathrm{D}}\left(\frac{\langle\sigma\rangle_{(i)}^{\mathrm{ult}}}{\sigma_0}\right) = \frac{i - 1/2}{N_{\mathrm{sim}}}, \tag{23}$$

for $i \in \{1,2,\ldots,N_{\mathrm{sim}}\}$. The 3D model of Fig. 2 is comprised of $2L_{3\mathrm{D}}\nu^2$ fibre segments, each of unit length. Therefore, the empirical weakest-link distribution associated with one fibre segment of unit length is given by:

$$W_{3\mathrm{D}}\left(\frac{\langle\sigma\rangle_{(i)}^{\mathrm{ult}}}{\sigma_0}\right) = 1 - \left(1 - H_{3\mathrm{D}}\left(\frac{\langle\sigma\rangle_{(i)}^{\mathrm{ult}}}{\sigma_0}\right)\right)^{\frac{1}{2L_{3\mathrm{D}}\nu^2}}. \tag{24}$$

In the sequel, wherever it is convenient to regard the empirical weakest-link distribution as a continuous function of the stress level, the subscript (i) is dropped, and the expression $W_{3\mathrm{D}}\left(\langle\sigma\rangle^{\mathrm{ult}}/\sigma_0\right)$ is used.

2.3 Two-dimensional model composite

Theories of 3D composite strength, e.g., Epstein (1948), Gücer and Gurland (1962), and Smith et al (1983), regard the 3D composite as a chain of mechanically non-interacting two-dimensional (2D) links arranged along the ζ direction. They identify the failure of the weakest 2D link with the failure of the 3D composite. A common feature of these models is that they assume the length of the 2D composites to be determined a priori, on the basis of mechanical considerations only. Furthermore, they restrict fibre breaks to a common transverse plane. It will be shown later in Sec. 4.4 that the aforementioned assumptions are too

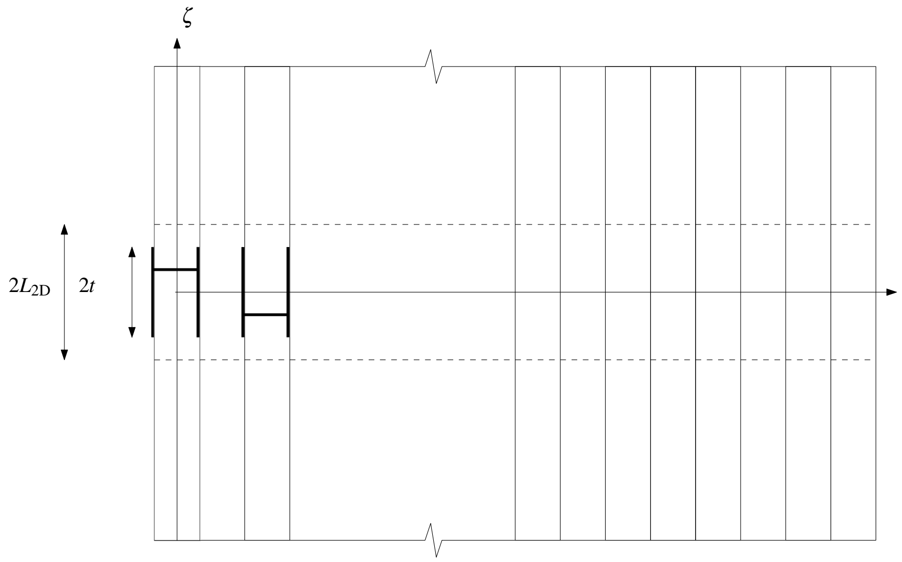

Fig. 3: Two-dimensional composite. Fibre breaks are assumed to be confined within $\zeta \in (-t,t)$, and matrix failures are assumed to extend over $\zeta \in (-t,t)$ in all the matrix bays abutting the broken fibres. Two fibre breaks in neighbouring fibres are shown. Although the common case of $2t < 2L_{2D}$ is depicted, there is no such restriction in general.

restrictive to accurately capture the size of the weakest-link failure event. This necessitates the definition of a broader class of 2D model composites.

The present 2D model composite is shown in Fig. 3. Fibre breaks are not restricted to a transverse plane. Instead, they may lie within $\zeta \in (-t,t)$. Matrix failures are assumed to extend over $\zeta \in (-t,t)$ in all the six matrix bays abutting each fibre break. A fibre break, and its abutting matrix failures, together are considered an aggregate failure event in the 2D composite. The aggregate failure is termed a 2D break. Two 2D breaks in neighbouring fibres are shown in Fig. 3. The traction-free boundary conditions associated with fibre breaks, and matrix failures imply that if there is a break in fibre (m,n), $\sigma_{mn}(\zeta) = 0$, for all $\zeta \in (-t,t)$, thereby making the precise location of the break within $\zeta \in (-t,t)$ immaterial.

The transverse section of the 2D composite is identical to that of the 3D composite. However, fibres (m,n) in the 2D composite are assumed infinitely long. The segment $\zeta \in (-L_{\mathrm{2D}}, L_{\mathrm{2D}})$ of fibre (m,n) is assigned a random Weibull (1952) distributed strength, $\Sigma_{mn}^{\mathrm{2D}}$:

$$F_{\mathrm{2D}}(\sigma) = \Pr\{\Sigma_{mn}^{\mathrm{2D}} \leq \sigma\} = 1 - \exp\left(-2L_{\mathrm{2D}}\left(\frac{\sigma}{\sigma_0}\right)^{\rho}\right). \tag{25}$$

The remainder of the infinitely long fibre is assumed to be infinitely strong.

It is recalled from Sec. 2.1 that the 3D model yields stress concentrations, σ_{mnk}, for arbitrary configurations of failed fibre and matrix elements. Consider a 3D composite with a broken fibre at $(m,n,\zeta) = (0,0,0)$, and with matrix failures extending up to $\zeta = \pm t$ in all the six abutting matrix bays. In the notation of Eq. 10, the stress overload induced in the fibre at (m,n) in the $\zeta = 0$ transverse plane is $\tilde{\sigma}_{mn0}$. $\tilde{\sigma}_{mn0}$ is taken to be the influence of the 2D break at $(m,n) = (0,0)$ Weighted superposition of the influences due to an arbitrary set of 2D breaks, following Hedgepeth (1961), yields the stress concentrations σ_{mn} in all the fibres. Presently, weighted influence superposition is done using the Fourier accelerated algorithm given by Gupta et al (2018).

2.4 Fracture simulation in 2D composites

Fracture simulations in 2D composites follow the procedure given in Sec. 2.2, barring three significant differences. First, in 2D, σ_{mn} increases monotonically with the number of 2D breaks, while in 3D, σ_{mnk} may vary non-monotonically. This property is exploited in the fast fracture simulation algorithm of Mahesh et al (2019), which is employed presently for 2D simulations. The second difference is that fracture simulations are performed assuming $2L_{\mathrm{2D}} = 1$. The empirical strength distributions so obtained are denoted $\hat{H}_{\mathrm{2D}}(\langle\sigma\rangle_{(i)}^{\mathrm{ult}}/\sigma_0)$. Using Eq. (25), the empirical strength distribution of a 2D composite of arbitrary length

$2L_{2D}$ is then obtained by scaling $\hat{H}_{2D}$ as

$$H_{2D}\left(\frac{\langle\sigma\rangle^{\rm ult}_{(i)}}{\sigma_0}\right)=\hat{H}_{2D}\left((2L_{2D})^{\frac{1}{\rho}}\frac{\langle\sigma\rangle^{\rm ult}_{(i)}}{\sigma_0}\right). \tag{26}$$

Thirdly, the condition for the occurrence of a 2D break in fibre (m,n) is taken as

$$\frac{\Sigma^{2D}_{mn}}{\sigma_0}\leq\sigma_{mn}\frac{\langle\sigma\rangle}{\sigma_0}. \tag{27}$$

Paralleling Eq. (24), the empirical weakest-link distribution of a 2D composite of length $2L_{2D}$, associated with one fibre segment of unit length is

$$\begin{aligned}W_{2D}\left(\frac{\langle\sigma\rangle^{\rm ult}_{(i)}}{\sigma_0}\right)&=1-\left(1-H_{2D}\left(\frac{\langle\sigma\rangle^{\rm ult}_{(i)}}{\sigma_0}\right)\right)^{\frac{1}{2L_{2D}v^2}},\\&=1-\left(1-\hat{H}_{2D}\left((2L_{2D})^{\frac{1}{\rho}}\frac{\langle\sigma\rangle^{\rm ult}_{(i)}}{\sigma_0}\right)\right)^{\frac{1}{2L_{2D}v^2}}.\end{aligned} \tag{28}$$

As in the 3D case, it is often simpler to regard the loading parameter, $\langle\sigma\rangle^{\rm ult}/\sigma_0$, as a continuous variable, and drop the subscript (i) in Eq. (28).

2.5 Longitudinal weakest linking

In accord with the classical theories of 3D composite strength, (Epstein 1948; Gücer and Gurland 1962; Smith et al 1983), it will be be shown in the sequel that the $2L_{3D}$ long 3D composite can be regarded as a chain of L_{3D}/L_{2D} links, each link representing a $2L_{2D}$-long 2D composite. Identifying the failure of the chain with that of the weakest link, it follows that

$$H_{3D}(\langle\sigma\rangle^{\rm ult}/\sigma_0)=1-\left(1-H_{2D}(\langle\sigma\rangle^{\rm ult}/\sigma_0)\right)^{L_{3D}/L_{2D}}. \tag{29}$$

Substituting Eqs. (24), and (28) into Eq. (29) gives

$$W_{3D}(\langle\sigma\rangle^{\rm ult}/\sigma_0)=W_{2D}(\langle\sigma\rangle^{\rm ult}/\sigma_0). \tag{30}$$

In the sequel, Eq. (30) will be found to offer a convenient way to verify the validity of Eq. (29).

3 Probabilistic models of fracture

Probabilistic models of fracture help to interpret empirical strength distributions obtained from Monte Carlo fracture simulations. Three models developed in the literature, relevant to the present work, are summarised below.

3.1 Equal load sharing model

In an equal load sharing bundle of v^2 fibres, of which b are broken (Hansen et al 2015),

$$\sigma_{mn}(\zeta) = \begin{cases} 0, & \text{in the broken fibres, and} \\ \frac{v^2}{v^2-b}, & \text{in the intact fibres.} \end{cases} \tag{31}$$

The 3D model composite of Fig. 2 represents an equal load sharing bundle if all the fibre-matrix interfaces were failed a priori, i.e., if $\tau_0/\sigma_0 = 0$. Similarly, in the limit of $t \to \infty$, the 2D model composite of Fig. 3 also represents an equal load sharing bundle. Thus, an equal load sharing bundle is defined irrespective of model dimensionality.

The strength distribution of an equal load sharing bundle comprised of v^2 fibres is denoted H_{ELS,v^2}. In the limit $v^2 \to \infty$, the classical result of Daniels (1945) holds that

$$H_{\mathrm{ELS},v^2}\left(\frac{\langle\sigma\rangle^{\mathrm{ult}}}{\sigma_0}\right) \xrightarrow{v^2\to\infty} \Phi\left(\frac{\langle\sigma\rangle^{\mathrm{ult}}/\sigma_0 - \mu_{v^2}/\sigma_0}{\varsigma_{v^2}/\sigma_0}\right), \tag{32}$$

where,

$$\Phi(x) = \sqrt{\frac{1}{2\pi}}\int_0^x e^{-x^2/2}dx, \tag{33}$$

is the Gaussian distribution with zero mean, and unit variance. The parameters of the Gaussian distribution, μ_{v^2}, and ς_{v^2}, given by Daniels (1945) converge slowly with increasing v^2. McCartney and Smith (1983) have proposed corrections that improve the rate of convergence. The corrected expressions for mean and variance, specialised to the case of Weibull distributed fibre strengths are

$$(2L_{\mathrm{x}})^{1/\rho}\frac{\mu_{\nu^2}}{\sigma_0} = \left(\frac{1}{\rho}\right)^{\frac{1}{\rho}} \exp\left(-\frac{1}{\rho}\right)\left\{1+\frac{0.996}{\nu^{4/3}}\frac{1}{2+\rho^{\frac{2}{\rho}}(\rho-2)}\right\}, \tag{34}$$

and

$$(2L_{\mathrm{x}})^{1/\rho}\varsigma_{\nu^2}^2 = \left(\frac{1}{\rho}\right)^{\frac{2}{\rho}} \frac{\exp\left(-\frac{1}{\rho}\right)\left(1-\exp\left(-\frac{1}{\rho}\right)\right)}{\nu^2} - \frac{0.317}{\nu^{8/3}}\left\{\frac{\left(\frac{1}{\rho}\right)^{-\frac{3}{\rho}}\exp(-\frac{1}{\rho})}{2+\rho^{\frac{2}{\rho}}(\rho-2)}\right\}^{2/3}, \tag{35}$$

respectively. Here, $L_{\mathrm{x}} = L_{3\mathrm{D}}$ for 3D and $L_{\mathrm{x}} = L_{2\mathrm{D}}$ for 2D equal load sharing bundles.

3.2 Localised load sharing models

While the fracture of an equal load sharing model composite is independent of its dimensionality, the localised load sharing models apply to transverse crack growth in 2D model composites only. The two models of present interest are the Curtin (1998) model, and the tight cluster growth model (Habeeb and Mahesh 2015; Gupta et al 2017; Kachhwah and Mahesh 2020).

3.2.1 The Curtin model

The Curtin (1998) model regards the 2D composite as a collection of ν^2/N_c bundles, each of which contains $N_c \leq \nu^2$ fibres. It assumes equal load sharing within each bundle. It associates composite failure with the failure of the weakest of the ν^2/N_c bundles. Let $H_{N_c}\left(\langle\sigma\rangle^{\mathrm{ult}}/\sigma_0\right)$ denote the strength distribution of an N_c bundle. Curtin (1998) observed that there is an N_c such that

$$H_{N_c}\left(\frac{\langle\sigma\rangle^{\mathrm{ult}}}{\sigma_0}\right) = 1-\left(1-H_{2\mathrm{D}}\left(\frac{\langle\sigma\rangle^{\mathrm{ult}}}{\sigma_0}\right)\right)^{\frac{1}{N_c}} = \Phi\left(\frac{\langle\sigma\rangle^{\mathrm{ult}}/\sigma_0-\mu'_{N_c}/\sigma_0}{\varsigma_{N_c}/\sigma_0}\right), \tag{36}$$

where, $H_{2D}(\langle\sigma\rangle^{\text{ult}}/\sigma_0)$ is defined in Sec. 2.4, and μ'_{N_c} is considered an arbitrary parameter, different from μ_{N_c} in Eq. (32). Two conditions must be satisfied if Eq. (36) were to hold: (i) H_{N_c} must Gaussian distributed, and (ii) Its standard deviation must coincide with that of an N_c fibre equal load sharing bundle. The following procedure for fitting N_c, and μ'_{N_c} attempts to optimally satisfy these conditions independently.

Given an empirical 2D strength distribution, $H_{2D}(\langle\sigma\rangle^{\text{ult}}/\sigma_0)$, trial H_{N_c} are calculated using Eq. (36) for each $N_c \in \{1, 2, \ldots, \nu^2\}$. $H_{2D}(\langle\sigma\rangle^{\text{ult}}/\sigma_0)$ is then plotted on normal probability paper, wherein Gaussian distributions plot as straight lines. A straight line is fit to the plot of $H_{2D}(\langle\sigma\rangle^{\text{ult}}/\sigma_0)$ using linear least squares. The root mean squared (RMS) deviation between the empirical $H_{2D}(\langle\sigma\rangle^{\text{ult}}/\sigma_0)$, and the straight line is used to quantify normality of $H_{2D}(\langle\sigma\rangle^{\text{ult}}/\sigma_0)$. The N_c for which the smallest RMS deviation results is taken to be the best fit parameter according to condition (i) above, and denoted $N_c^{(\text{i})}$. The reciprocal of the slope of the best fit straight line gives the standard deviation of the normal distribution. Its absolute deviation from the standard deviation given by Eq. (35), quantifies the satisfaction of condition (ii). The N_c for which absolute deviation is minimum is taken to be the best fit parameter according to condition (ii) above, and denoted $N_c^{(\text{ii})}$. Curtin (1998) observed that $N_c^{(\text{i})} \approx N_c^{(\text{ii})}$. Finally, the parameter μ'_{N_c} is set by determining the horizontal shift in normal probability paper required to bring $H_{2D}(\langle\sigma\rangle^{\text{ult}}/\sigma_0)$, and $\Phi((\langle\sigma\rangle^{\text{ult}}/\sigma_0) - \mu'_{N_c}/\sigma_0)/(\varsigma_{N_c}/\sigma_0))$ into best alignment with each other.

3.2.2 The tight cluster growth model

The tight cluster growth model (Habeeb and Mahesh 2015; Gupta et al 2017; Kachhwah and Mahesh 2020) regards the 2D composite as a collection of ν^2/M bundles, each of which contains $M \leq \nu^2$ fibres. Like the Curtin (1998) model, it assumes equal load sharing within

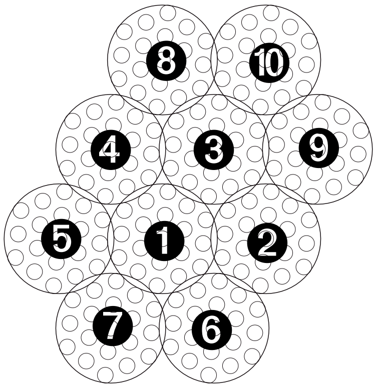

Fig. 4: Schematic representation of the failure event in the tight cluster growth model. The failure of a bundle, labelled ❶, causes an overload in its six neighbours. Under this overload, one of them, say ❷ fails. The overloads due to a pair of failed bundles leads to the failure of, say ❸, and so on.

each bundle. However, following Smith et al (1983), and Mahesh et al (2002), it assumes that brittle fracture develops by tight cluster growth.

Tight cluster growth is taken to begin from a state of uniformly randomly distributed fibre breaks. The random distribution is taken to increase the mean stress in every transverse section by a factor $K_{\mathrm{rand}} \gtrapprox 1$. Cluster growth begins with the failure of one bundle, the nucleus under stress per fibre $K_{\mathrm{rand}}\langle\sigma\rangle^{\mathrm{ult}}/\sigma_0$. This induces stress concentrations on the neighbours of the bundle, causing at least one of them to fail. Tight cluster growth propagates by the failure of at least one its most overloaded neighbours of the current set of failed bundles. One of the possible routes of fracture development is shown in Fig. 4. The probability of tight cluster growth starting from a given M-bundle nucleus is (Kachhwah and Mahesh 2020)

$$H_M\left(\frac{\langle\sigma\rangle^{\mathrm{ult}}}{\sigma_0}\right) = \prod_{j=0}^{\lfloor \nu^2/M \rfloor - 1} \left\{1 - \left(1 - H_{\mathrm{ELS},M}\left(K_{\mathrm{rand}}\sigma_j^* \frac{\langle\sigma\rangle^{\mathrm{ult}}}{\sigma_0}\right)\right)^{n_j}\right\}. \tag{37}$$

Here, $H_{\mathrm{ELS},M}$ is given by Eq. (32) with $\nu^2 = M$, and $L_\mathrm{x} = 2L_{\mathrm{2D}}$, and σ_j^* and n_j denote the maximum stress concentration and the number of nearest neighbours of a tight cluster of j M-bundles, respectively. The computation of σ_j^* and n_j is described in detail in Kachhwah and Mahesh (2020, § II.B.2). $\sigma_0^* = n_0 = 1$. The weakest-link model strength distribution referred to one fibre segment of unit length is:

$$W_M\left(\frac{\langle\sigma\rangle^{\mathrm{ult}}}{\sigma_0}\right) = 1 - \left(1 - H_M\left(\frac{\langle\sigma\rangle^{\mathrm{ult}}}{\sigma_0}\right)\right)^{\frac{1}{2L_{\mathrm{2D}}M}}. \tag{38}$$

The parameters of the tight cluster growth model are M, and K_{rand}. Given an empirical 2D strength distribution, $H_{\mathrm{2D}}(\langle\sigma\rangle^{\mathrm{ult}}/\sigma_0)$, Eq. (28) is used to obtain the weakest-link distribution, $W_{\mathrm{2D}}(\langle\sigma\rangle^{\mathrm{ult}}/\sigma_0)$. For each $M \in \{1, 2, \ldots, \nu^2\}$, trial W_M are calculated using Eq. (38). For each M, K_{rand} is fit using successive bisection so as to minimise the RMS error between W_M and W_{2D}. The (M, K_{rand}) for which the least RMS error is obtained are taken to be the best fit parameters.

4 Results and discussion

Monte Carlo simulations of the fracture of three-dimensional model composites are performed for specimen sizes $\nu^2 \in \{2^8, 2^{10}, 2^{12}\}$, Weibull exponents, $\rho \in \{10, 20\}$, and for various deterministic normalised matrix strengths, $0 \le \tau_0/\sigma_0 \le \infty$. For each $(\nu^2, \rho, 2L_{\mathrm{3D}}, \tau_0/\sigma_0)$, 3D fracture simulations are repeated on $N_{\mathrm{sim,3D}} = 256$ statistically identical model specimen. Using the ultimate tensile strengths, $\langle\sigma\rangle^{\mathrm{ult}}_{(i)}$, obtained from these simulations, the empirical weakest-link strength distribution, $W_{3D}(\langle\sigma\rangle^{\mathrm{ult}}_{(i)}/\sigma_0)$, is calculated from Eqs. (23) and (24).

Monte Carlo simulations of the fracture of two-dimensional composite specimen with $2L_{\mathrm{2D}} = 1$, $\nu^2 \in \{2^8, 2^{10}, 2^{12}\}$, and $\rho \in \{10, 20\}$ are also performed. Empirical 2D strength distributions, $\hat{H}_{\mathrm{2D}}(\langle\sigma\rangle^{\mathrm{ult}}_{(i)}/\sigma_0)$, are obtained for

$$t \in \{0, 0.05, 0.10, \ldots, 1.20, 1.25\}. \tag{39}$$

As 2D simulations are typically much faster than the 3D ones, $N_{\mathrm{sim,2D}} = 1024$ statistically identical 2D realisations are tested in the computer for each $(\nu^2, \rho, 2L_{\mathrm{2D}}, t)$. Eq. (28) is used to obtain the empirical weakest-link strength distribution, $W_{\mathrm{2D}}(\langle\sigma\rangle^{\mathrm{ult}}_{(i)}/\sigma_0)$.

Below, the empirical strength distributions from the 3D simulations are interpreted using those from the 2D simulations, and those from the 2D simulations are interpreted in terms of the stochastic models of Sec. 3.2. For logical development, the latter is presented first.

4.1 Transverse size of the weakest-link in 2D model composites

The parameters N_c, and M, of the Curtin (1998), and tight cluster growth models, summarised in Sec. 3.2, respectively, represent the transverse size of the weakest-link in the 2D model composites. Presently, these parameters are estimated from 2D simulations of $2L_{\mathrm{2D}} = 1$ specimen.

4.1.1 Curtin's model

The algorithmic procedure for obtaining the best fit parameters (N_c, μ'_{N_c}) of the Curtin (1998) model is given in Sec. 3.2.1. It produces two values of N_c, viz., $N_c^{\mathrm{(i)}}$, and $N_c^{\mathrm{(ii)}}$, depending on the criterion used for selecting the best fit.

Consider the $(\nu^2, \rho, 2L_{\mathrm{2D}}, t) = (2^{10}, 10, 1, 0.3)$ 2D model specimen. Fig. 5a shows the errors calculated according to conditions (i) and (ii). The best fit values are $N_c^{\mathrm{(i)}} = 254$, and $N_c^{\mathrm{(ii)}} = 111$, respectively. Clearly, $N_c^{\mathrm{(i)}} \not\approx N_c^{\mathrm{(ii)}}$, contrary to the observation of Curtin (1998).

Fig. 5b shows $H_{N_c^{\mathrm{(i)}}}$ for $N_c^{\mathrm{(i)}} = 254$ on normal probability paper, and the best fit straight line passing through the empirical distribution. Also shown is $H_{\mathrm{ELS},N_c^{\mathrm{(i)}}}$, given by Eq. (32). It is evident that $H_{N_c^{\mathrm{(i)}}} \not\approx H_{\mathrm{ELS},N_c^{\mathrm{(i)}}}$. Also shown in this figure are $H_{N_c^{\mathrm{(ii)}}}$, and the $H_{\mathrm{ELS},N_c^{\mathrm{(ii)}}}$

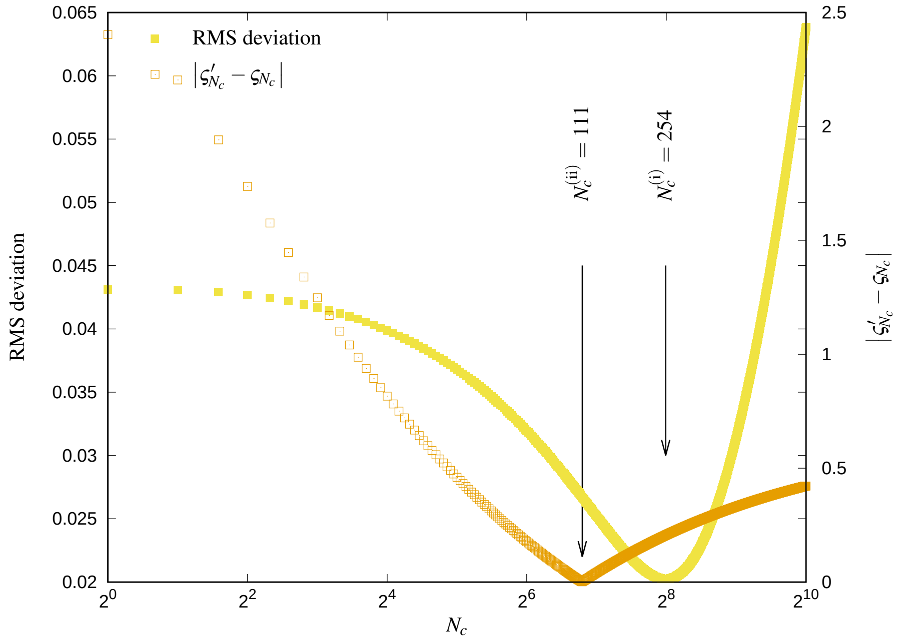

(a)

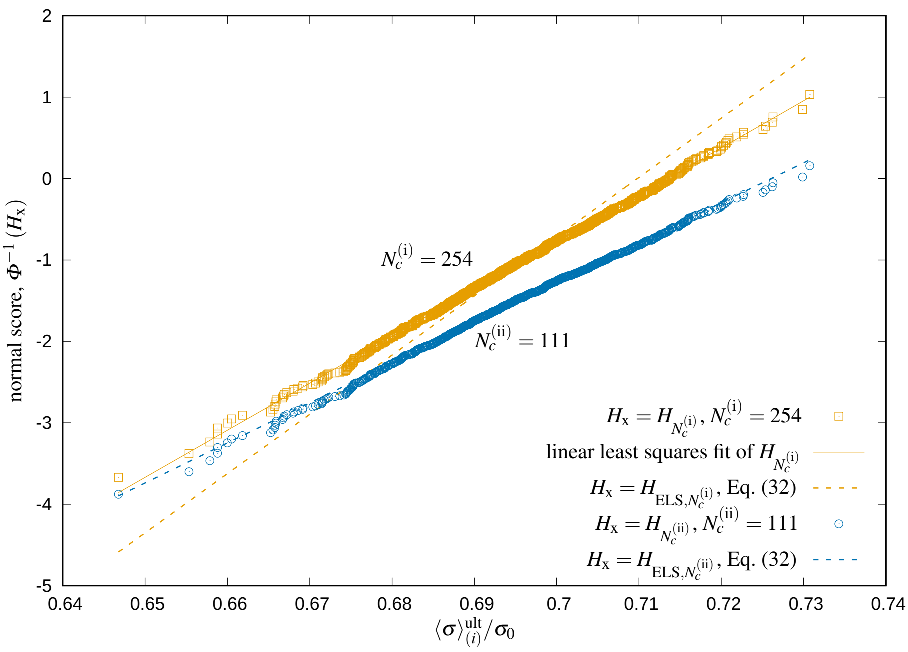

(b)

Fig. 5: For 2D composites with $(v^2, \rho, 2L_{2\mathrm{D}}, t) = (2^{10}, 10, 1, 0.3)$, (a) selection of the optimal N_c that satisfies Eq. (36). Two optima, $N_c^{(\mathrm{i})}$, and $N_c^{(\mathrm{ii})}$, are obtained corresponding to the two criteria in Sec. 3.2.1, and (b) comparison of H_{N_c} with H_{ELS,N_c} on normal probability paper.

that has been brought into alignment with it by choosing an appropriate $\mu'_{N_c^{(\mathrm{ii})}}$. Although $H_{\mathrm{ELS}],N_c^{(\mathrm{ii})}}$ is not the normal distribution that best fits $H_{N_c^{(\mathrm{ii})}}$, this is not visually perceptible.

Thus, $H_{N_c^{(\mathrm{i})}}$ optimally satisfies criterion (i) associated with Eq. (36), but violates criterion (ii) by a large margin. $H_{N_c^{(\mathrm{ii})}}$ optimally satisfies criterion (ii), and also acceptably satisfies criterion (i). This is found to be generally true for all $(\nu^2, \rho, 2L_{\mathrm{2D}}, t)$. Therefore, N_c is taken to be $N_c^{(\mathrm{ii})}$ hereafter.

4.1.2 *Tight cluster growth model*

Fig. 6 shows the empirical weakest-link strength distributions, W_{2D}, for model 2D composites, with $\rho = 10$, and $2L_{\mathrm{2D}} = 1$. Tight cluster growth model predictions, W_M, are obtained by fitting Eq. (38), as described in Sec. 3.2.2.

Fig. 6 shows the good agreement between the model predicted W_{M}, and W_{2D} for $t = 0.3$, and $t = 0.7$. In general, for all $(\nu^2, \rho, 2L_{\mathrm{2D}}, t)$, the model predictions are found to fit W_{2D} very well.

4.2 The effect of fibrewise discretisation length, Δ

Attention is henceforth directed toward 3D model composites. The fibrewise discretisation length, Δ, shown in Fig. 2, influences the 3D empirical strength distributions $W_{3D}(\langle\sigma\rangle^{\mathrm{ult}}_{(i)}/\sigma_0)$. Curtin (2000) has discussed the effect of restricting the fibre breaks to a discrete set of transverse planes spaced one load recovery length apart for the case of frictional load transfer across the fibre-matrix interface. He found that the restriction made the model composites significantly weaker, and increased their strength variability. However, Curtin (2000) did not investigate the effect of decreasing the spacing, Δ, between the transverse planes. Landis et al (2000) studied the effect of decreasing Δ in model composites with perfect

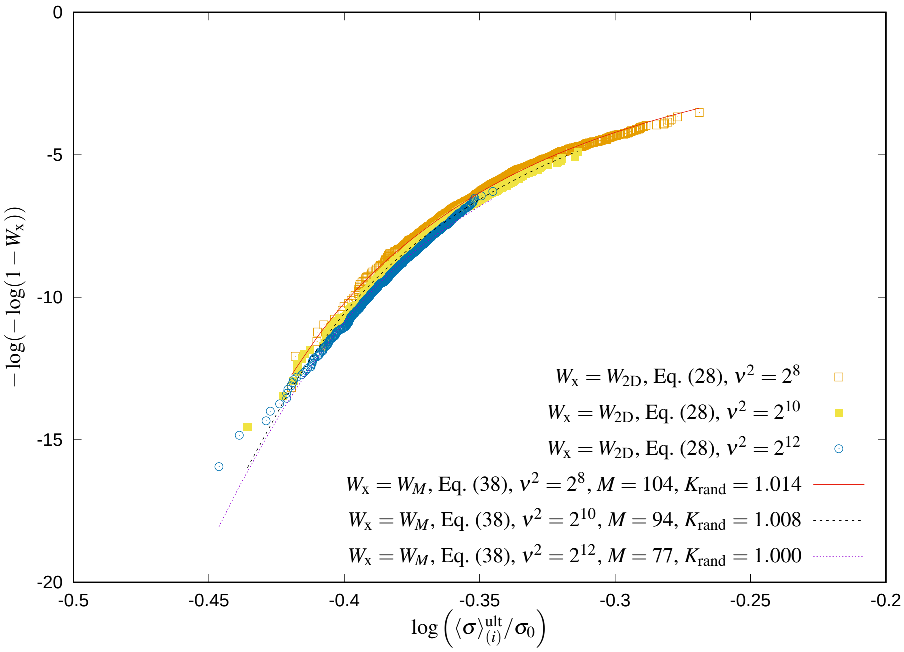

(a) $t = 0.3$

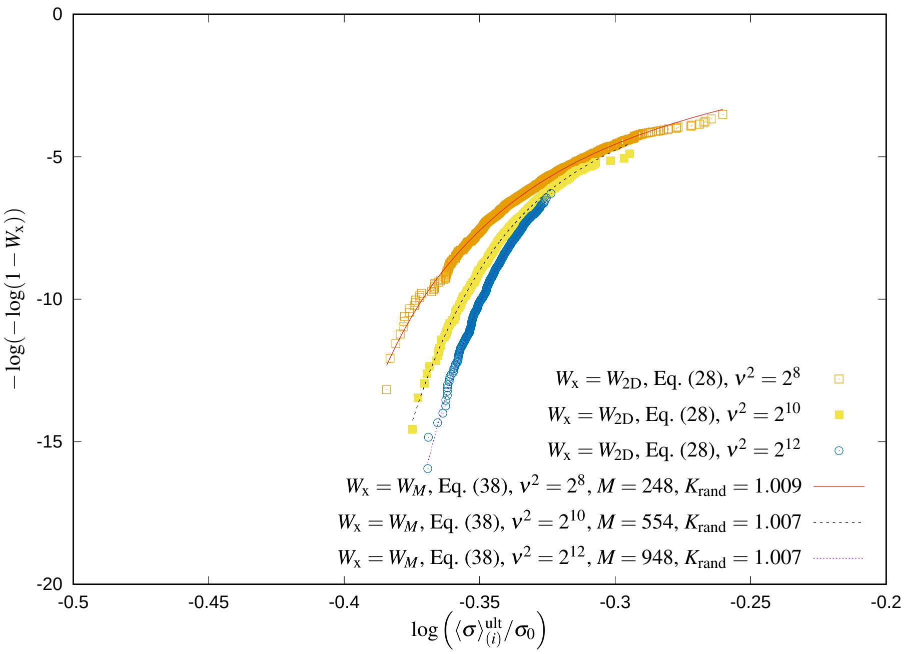

(b) $t = 0.7$

Fig. 6: Comparison of the 2D empirical weakest-link distribution, Eq. (28), obtained for $2L_{2D} = 1.0$ with the best fit tight cluster growth model predictions given by Eq. (38), for (a) $t = 0.3$, and (b) $t = 0.7$.

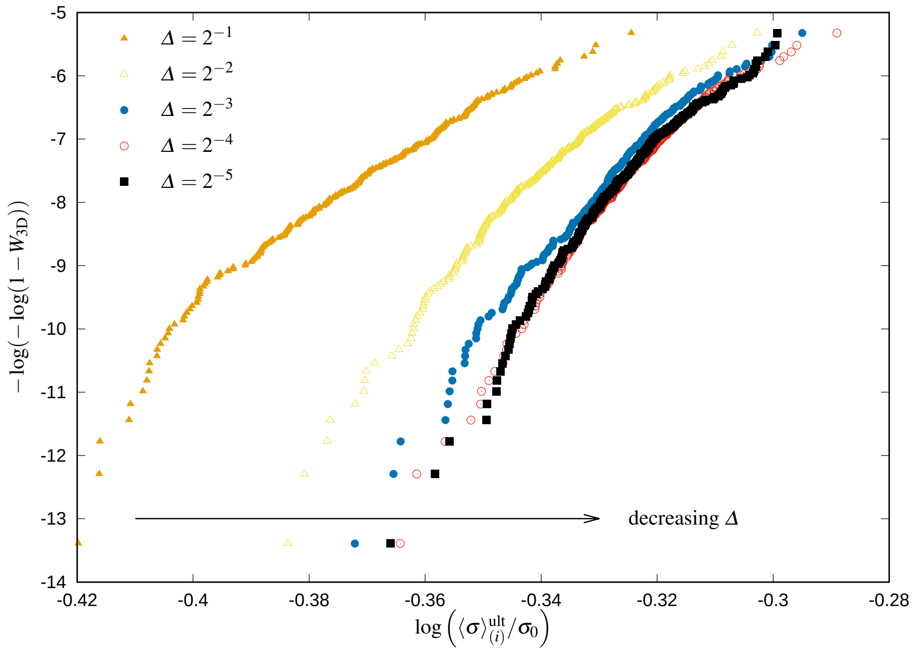

Fig. 7: Weakest-link empirical strength distributions obtained for $(\nu^2, \rho, 2L_{3D}, \tau_0/\sigma_0) = (2^8, 10, 5, \infty)$ composites. Successively halving the fibre-wise discretisation length, Δ, eventually leads to convergence of the empirical distributions.

interfacial bonding. They found that as Δ decreases, the predicted empirical strengths converge in distribution. They obtained a slower convergence rate for fibre breaks restricted to evenly-spaced transverse planes than for arbitrarily located breaks.

The fast stress redistribution algorithm developed in Mahesh (2020) requires the fibre breaks to be located in a regular grid, so that positioning fibre breaks arbitrarily is infeasible. Therefore, convergence of the empirical distributions with decreasing Δ, with the fibre breaks restricted to a regular grid is now considered.

Consider a $(\nu^2, \rho, 2L_{3D}, \tau_0/\sigma_0) = (2^8, 10, 5, \infty)$ composite with a perfect interface, as in Landis et al (2000). Fig. 7 shows the effect of decreasing Δ from 2^{-1} to 2^{-5} in multiplicative

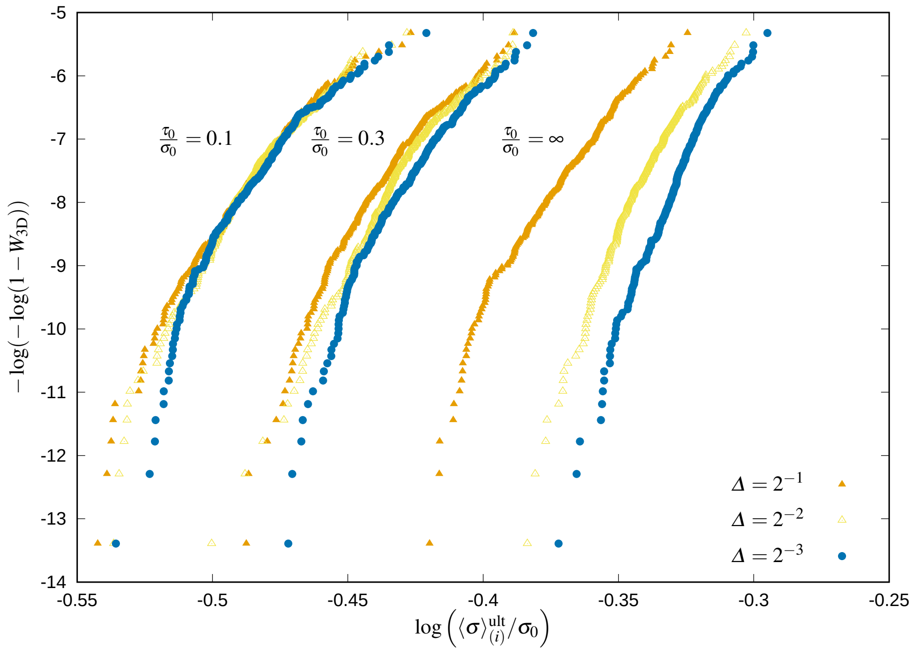

Fig. 8: Weakest-link empirical strength distributions for 3D model composites $W_{3D}(\langle\sigma\rangle^{\rm ult}_{(i)}/\sigma_0)$, Eq. (24), obtained for $(\nu^2, 2L_{3D}) = (2^8, 5)$ composites, with interfacial strength $\tau_0/\sigma_0 \in \{0.1, 0.3, \infty\}$. The distributions converge more rapidly with decreasing τ_0/σ_0.

steps of 2^{-1} on the weakest-link distribution. In accord with the observations of Curtin (2000), and Landis et al (2000) the model composite strengthens with decreasing Δ. The weakest-link distributions approach each other with decreasing Δ, indicating convergence in distribution.

The strengthening of the composite with decreasing Δ can be understood as follows. Consider two model composites with fibrewise discretisation lengths Δ_1, and Δ_2, obeying $\Delta_1 > \Delta_2$. Let there be the same number of arbitrarily located breaks in both. In the present computational scheme these breaks are relocated to the block boundaries. In the Δ_1 composite, the average number of breaks on a block boundary will be greater than in the Δ_2 composite. Therefore, stress concentrations in the former will be greater, which increases the likelihood of crack propagation. Conversely, the greater fibrewise staggering of breaks in the Δ_2 composite diminishes the stress overloads they produce on the intact fibres. This renders the Δ_1 model composite weaker than the Δ_2 composite.

Fig. 8 shows the 3D empirical weakest-link distributions obtained for $(v^2, \rho, 2L_{3D}) = (2^8, 10, 5)$ composites corresponding to $\tau_0/\sigma_0 \in \{0.1, 0.3, \infty\}$, and $\Delta \in \{2^{-1}, 2^{-2}, 2^{-3}\}$. It is seen that the rate of distributional convergence increases with decreasing τ_0/σ_0. This is consistent with the limiting case of equal load sharing, $\tau_0/\sigma_0 = 0$, wherein the fibrewise position of the fibre breaks, and therefore, Δ, is immaterial.

Figs. 7, and 8 suggest performing simulations with small enough $\Delta(\tau_0/\sigma_0)$ at which the weakest-link distribution has converged. This varies from $\Delta = 2^{-4}$ for $\tau_0/\sigma_0 = \infty$ to $\Delta = 2^{-1}$ for $\tau_0/\sigma_0 = 0.1$. However, the fine discretisation required at larger τ_0/σ_0 increases the computational cost of the larger v^2 simulations prohibitively. In order to complete the simulations with the available computational resources, all the simulations discussed hereafter are performed keeping $\Delta = 2^{-2}$ fixed. This implies that the composite strengths so obtained are conservative underestimates, with the degree of underestimation increasing with increasing τ_0/σ_0.

4.3 Weakest link scaling

In Fig. 9 the empirical $W_{3D}(\langle\sigma\rangle^{\text{ult}}_{(i)}/\sigma_0)$, for $(v^2, \rho, 2L_{3D}) = (v^2, 10, 5)$ model composites for $v^2 \in \{2^8, 2^{10}, 2^{12}\}$, and $\tau_0/\sigma_0 \in \{0.0, 0.3, 0.5, 0.7, \infty\}$ are shown. The empirical strength distributions corresponding to $\tau_0/\sigma_0 = 0.7$, and $\tau_0/\sigma_0 = \infty$ coincide exactly. $\tau_0/\sigma_0 = 0$, and $\tau_0/\sigma_0 = \infty$ correspond to equal load sharing, and perfect interfacial bonding, respectively.

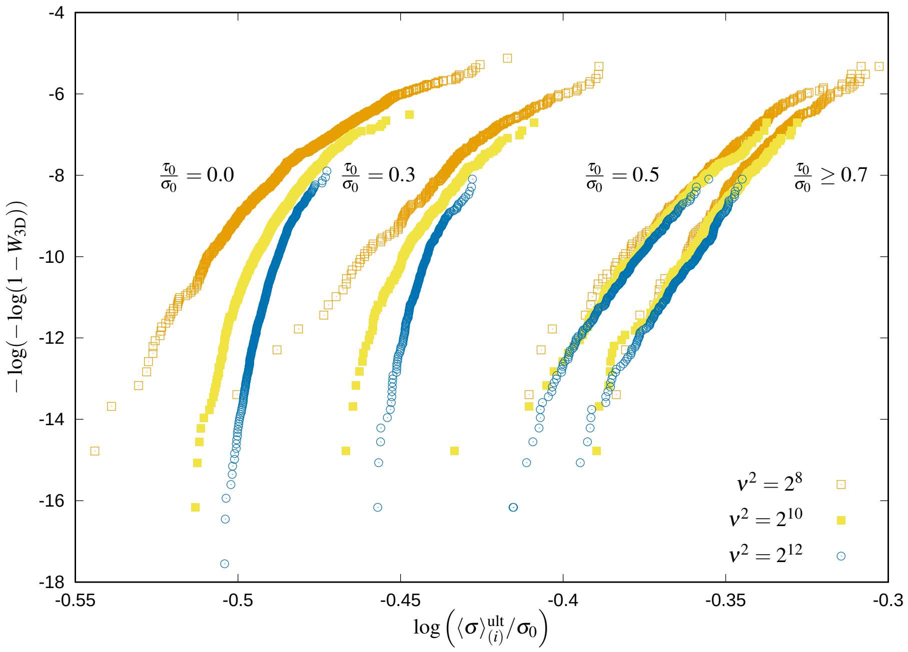

Fig. 9: Weakest-link 3D empirical strength distributions, W_{3D}, obtained for $(\rho, 2L_{3D}) = (10, 5)$ composites with $v^2 \in \{2^8, 2^{10}, 2^{12}\}$ fibres, and various τ_0/σ_0. W_{3D} for all $\tau_0/\sigma_0 \geq 0.7$ coincide. $\tau_0/\sigma_0 = 0$ refers to equal load sharing.

Composite strength is seen to decrease monotonically with decreasing τ_0. W_{3D} corresponding to $v^2 \in \{2^8, 2^{10}, 2^{12}\}$ for $\tau_0/\sigma_0 \geq 0.5$ collapse onto a common curve, while those for $\tau_0/\sigma_0 \in \{0, 0.3\}$ do not. The collapse for $\tau_0/\sigma_0 \geq 0.5$ indicates the validity of weakest-link scaling (Smith 1980). It suggests that brittle fracture develops by the occurrence of a localised weakest-link failure event, and its almost sure propagation (Harlow and Phoenix 1981a,b). However, non-coincidence of W_{3D} for $\tau_0/\sigma_0 \in \{0, 0.3\}$ does not unequivocally indicate the tough failure mode, because apparent toughness may also arise from the limited size of the model composites. It is known that brittle fracture from a weakest-link can be suppressed in fracture simulations if the model composite size were comparable to, or

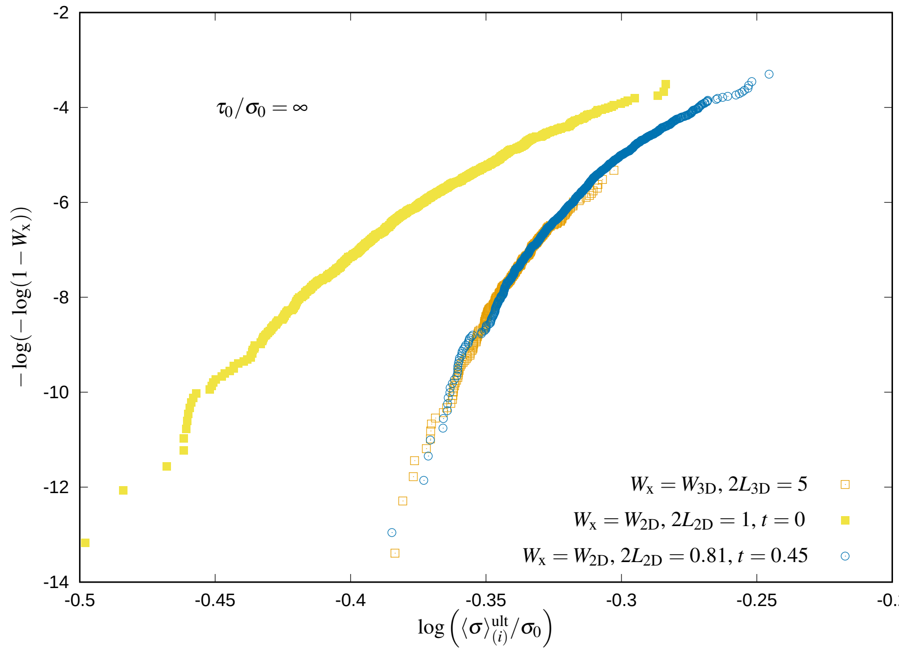

Fig. 10: Attempts to match the 3D and 2D empirical weakest-link strength distributions for $\nu^2 = 2^8$ fibre, $\rho = 10$ model composites with a perfect interface. The 2D empirical weakest-link strength distribution assuming no interfacial debonding does not match the 3D one. However, good agreement between the 2D and 3D distributions is obtained for non-zero $t = 0.45$.

smaller than the size of the weakest-link failure event (Mahesh et al 2002, 2019). A novel method that unequivocally determines the fracture mode for all τ_0/σ_0 is now developed. It is based on estimating the size of the weakest-link failure event, and its scaling with composite size.

4.4 Fibrewise length of the weakest link

Consider a 3D composite with a perfect interface. Smith (1980) and Smith et al (1983) proposed that the composite could be regarded as a chain of 2D composite 'links', each of unit length. They assumed that the 2D composite links fail independently, and associated the failure of the 3D composite with that of the weakest 2D link.

Fig. 10 shows the empirical 3D weakest-link strength distribution $W_{3\mathrm{D}}(\langle\sigma\rangle^{\mathrm{ult}}_{(i)}/\sigma_0)$ of $(v^2,\rho,2L_{3\mathrm{D}}) = (2^8,10,5)$ composites with perfect interfaces. Also shown are the empirical weakest-link strength distributions, $W_{2\mathrm{D}}$, corresponding to 2D $(v^2,\rho,2L_{2\mathrm{D}},t) = (2^8,10,1,0)$ model composites. These 2D model composites were proposed by Smith et al (1983) as the longitudinal weakest-link. If indeed they were, $W_{3\mathrm{D}}$, and $W_{2\mathrm{D}}$ must coincide, obeying Eq. (30). However, the 2D weakest-link is clearly weaker than that of the 3D composite. This indicates that 2D weakest link proposed by Smith et al. is too conservative.

It is now attempted to satisfy Eq. (30) by allowing arbitrary $2L_{2\mathrm{D}} \geq 0$, and $t \geq 0$ in the 2D model, as described in Sec. 2.3. In fact, for a given $(v^2,\rho,2L_{3\mathrm{D}},\tau_0/\sigma_0)$ 3D model composite, the $(v^2,\rho,2L_{2\mathrm{D}},t)$ 2D model composite that best satisfies Eq. (30) can be determined algorithmically follows. For each t given by Eq. (39), and $2L_{2\mathrm{D}} = 1$, smooth model fits of $W_{2\mathrm{D}}$ are already available from Sec. 4.1. Either of these model fits can be scaled to arbitrary $2L_{2\mathrm{D}}$ using Eq. (26). For fixed t, the RMS error between the scaled distribution and $W_{3\mathrm{D}}$ can be minimised efficiently using successive bisection over $2L_{2\mathrm{D}}$, starting with the initial bracket $2L_{2\mathrm{D}} \in [0,2L_{3\mathrm{D}}]$ to obtain the optimal length, $2L^*_{2\mathrm{D}}(t)$. Repeating the minimisation for all t in Eq. (39) and choosing the t^*, and $2L^*_{2\mathrm{D}}(t^*)$ which yield minimum RMS error between $W_{3\mathrm{D}}$, the $(v^2,\rho,2L^*_{2\mathrm{D}},t^*)$ parameters of the 2D composite 'link' that best satisfies Eq. (30) are determined.

Applying this procedure to the $W_{3\mathrm{D}}$ of Fig. 10 yields the optimal parameters $t^* = 0.45$, and $2L^*_{2\mathrm{D}} = 0.81$. The resulting $W_{2\mathrm{D}} \approx W_{3\mathrm{D}}$, in accord with Eq. (30). This confirms the longitudinal weakest-link scaling of Eq. (29). Although matrix failure does not occur in the 3D model composites of Fig. 10 with perfect fibre-matrix interfaces, $W_{3\mathrm{D}}$ is fit well by a $W_{2\mathrm{D}}$ that assumes matrix failure. Thus, t^* in the 2D model does not represent a physical feature in the fracture of the 3D model. Instead, t^* effectively captures the reduced stress concentration in the 3D model due to longitudinally staggered breaks, as discussed in connection with Fig. 7. The present result also makes clear that the conservative character of the predictions from the Smith et al (1983) model arises from underestimating the fibrewise staggering of the fibre breaks, or overestimating the stress overloads.

For all $(\nu^2, \rho, 2L_{3\mathrm{D}}, \tau_0/\sigma_0)$ 3D composites presently considered, it is found that the algorithm given above results in $(\nu^2, \rho, 2L^*_{2\mathrm{D}}, t^*)$ 2D 'link' parameters that satisfy Eq. (30). Fig. 11 shows the fits obtained for $(\rho, 2L_{3\mathrm{D}}) = (10, 5)$ 3D simulations with $\nu^2 \in \{2^8, 2^{10}, 2^{12}\}$, and $\tau_0/\sigma_0 \in \{0.3, 0.5\}$. It is seen that the fits are very good, irrespective of whether $W_{3\mathrm{D}}$ obeys weakest-link scaling. The parameter t^* in these fits captures two effects: that of fibrewise fibre break staggering, and of physical matrix failure. The parameter $2L^*_{2\mathrm{D}}$ represents the longitudinal size of the weakest-link failure event.

4.5 Tough-brittle transition

The weakest-link failure event has transverse size, N_c, or M, determined in Sec. 4.1, and longitudinal size, $2L^*_{2\mathrm{D}}$, determined in Sec. 4.4. The scaling of these sizes with the number of fibres, ν^2, is presently examined in order to infer whether the fracture mode is tough or brittle. The fractional size of the fracture nucleus according to the Curtin (1998), and tight cluster growth models, are N_c/ν^2, and M/ν^2. If the fracture mode were brittle, N_c, and M

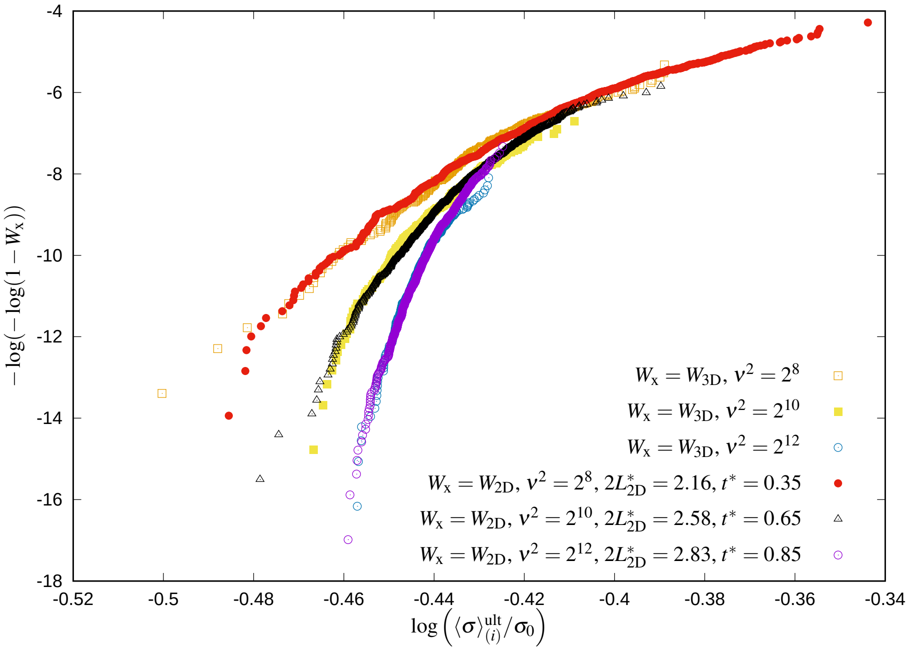

(a) $\tau_0/\sigma_0 = 0.3$

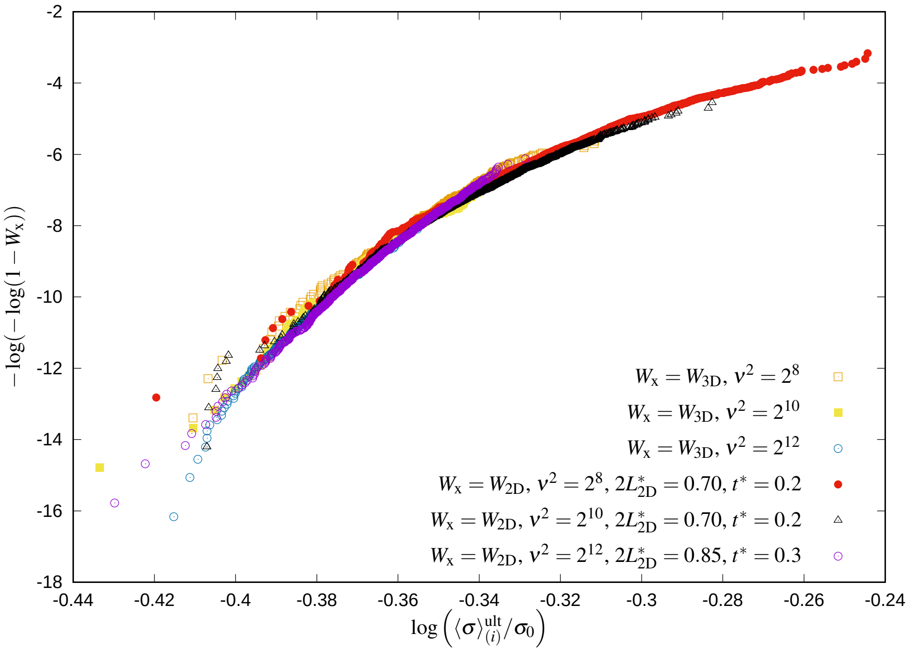

(b) $\tau_0/\sigma_0 = 0.5$

Fig. 11: Fits of the 2D weakest link distributions, W_{2D}, to the 3D weakest-link strength distributions, W_{3D}, for (a) $\tau_0/\sigma_0 = 0.3$, and (b) $\tau_0/\sigma_0 = 0.5$. $\rho = 10$, and $2L_{3D} = 5$. The characteristic parameters $(2L^*_{2D}, t^*)$ of the best fitting 2D model are listed in the legend.

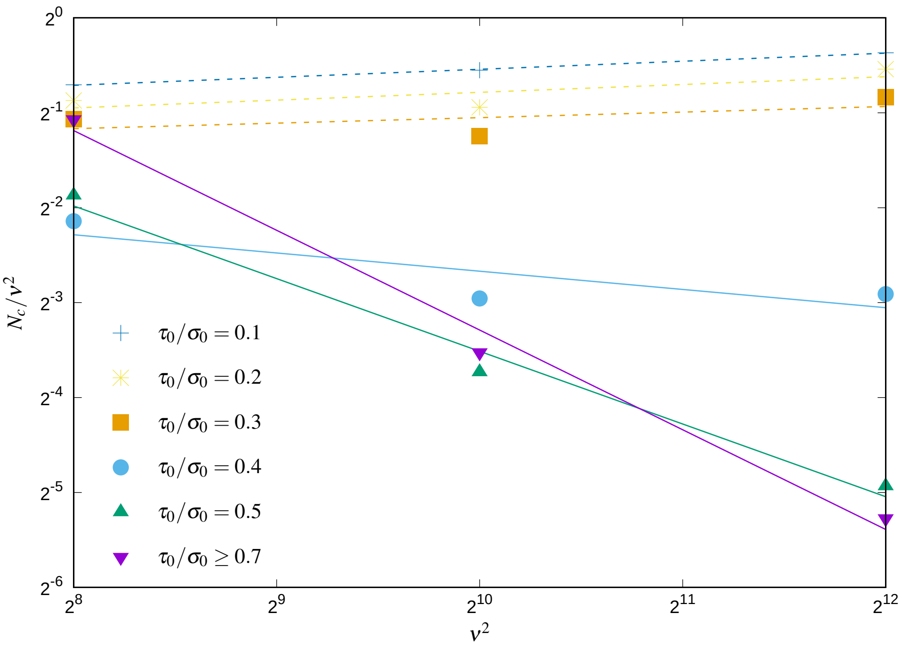
2^0
2^{-1}
2^{-2}
2^{-3}
2^{-4}
2^{-5}
2^{-6}
N_c/v^2
2^8
2^9
2^{10}
2^{11}
2^{12}
v^2
$\tau_0/\sigma_0 = 0.1$
$\tau_0/\sigma_0 = 0.2$
$\tau_0/\sigma_0 = 0.3$
$\tau_0/\sigma_0 = 0.4$
$\tau_0/\sigma_0 = 0.5$
$\tau_0/\sigma_0 \geq 0.7$

(a)

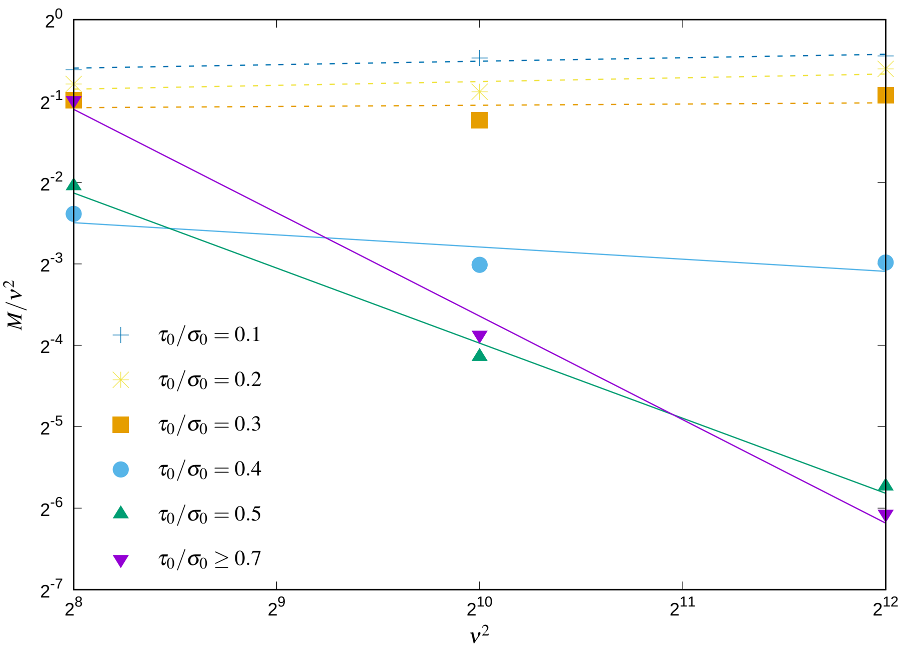
2^0
2^{-1}
2^{-2}
2^{-3}
2^{-4}
2^{-5}
2^{-6}
2^{-7}
M/v^2
2^8
2^9
2^{10}
2^{11}
2^{12}
v^2
$\tau_0/\sigma_0 = 0.1$
$\tau_0/\sigma_0 = 0.2$
$\tau_0/\sigma_0 = 0.3$
$\tau_0/\sigma_0 = 0.4$
$\tau_0/\sigma_0 = 0.5$
$\tau_0/\sigma_0 \geq 0.7$

(b)

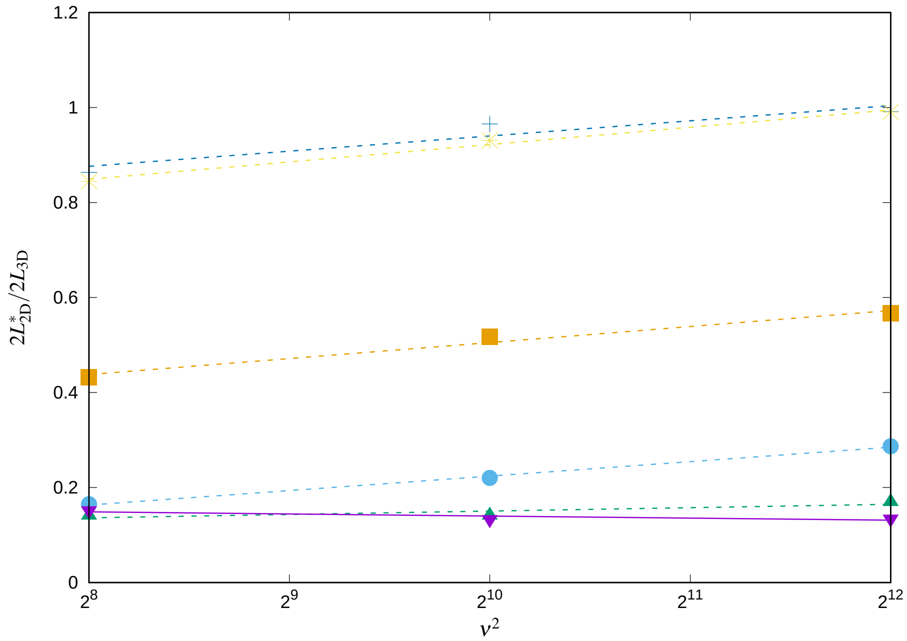

(c)

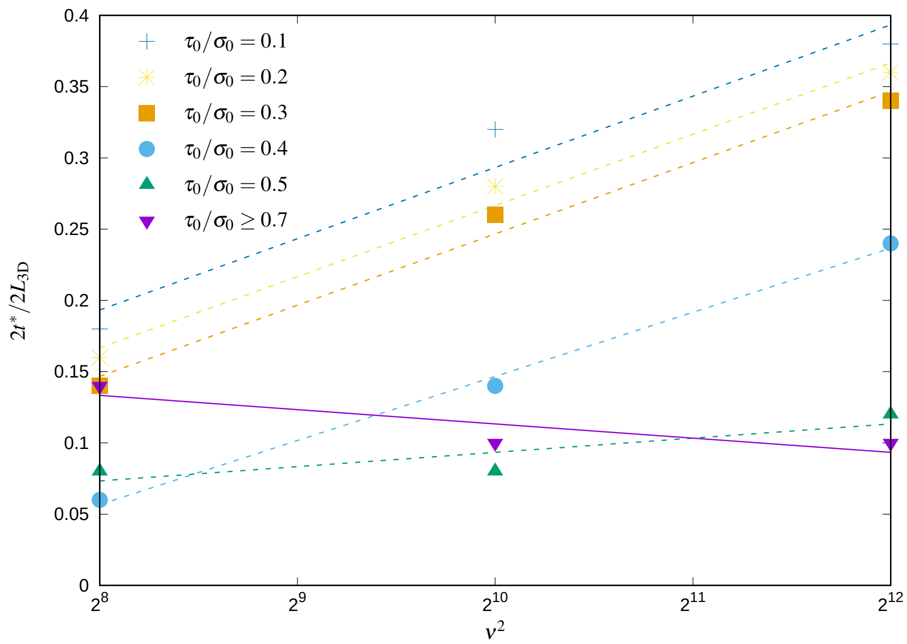

(d)

Fig. 12: Scaling of (a) the fractional transverse size N_c/ν^2 according to the Curtin (1998) model, (b) the fractional transverse size M/ν^2 according to the tight cluster growth model, (c) the fractional longitudinal size $2L^*_{\mathrm{2D}}/2L_{\mathrm{3D}}$, and (d) the effective length of matrix failure, $2t^*/2L_{\mathrm{3D}}$, in $(\rho, 2L_{\mathrm{3D}}) = (10, 5)$ 3D composites with the number of fibres, ν^2. Lines represent linear least squares fits of the points. Lines with positive and negative slopes are drawn dashed, and solid, respectively. The legend is the same in all the figures (a)–(d).

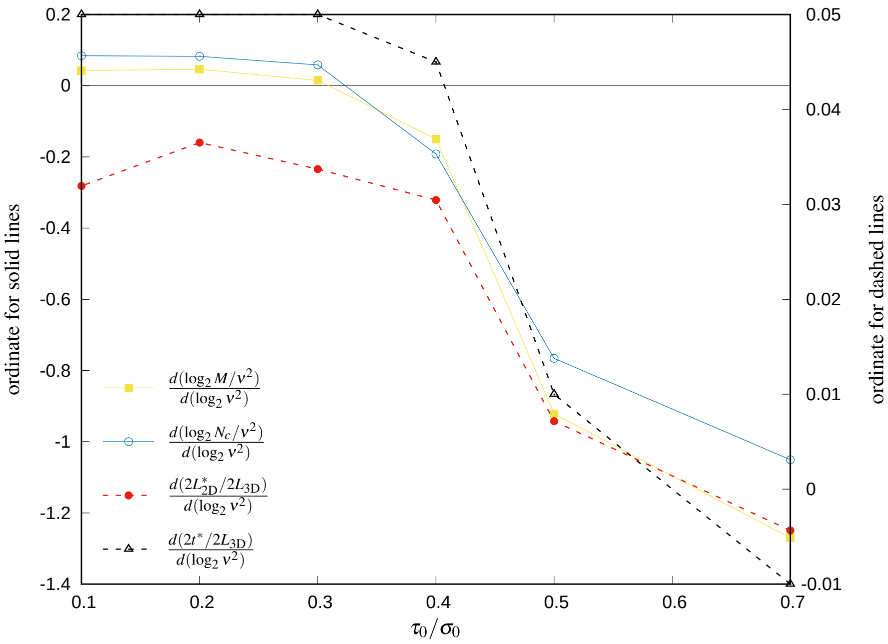

Fig. 13: Variation with τ_0/σ_0 of the slopes of the straight line fits of Fig. 12, for $\rho = 10$ composites. The ordinates of the $d(\log_2 M/\nu^2)/d(\log_2 \nu^2)$, and $d(\log_2 N_c/\nu^2)/d(\log_2 \nu^2)$ curves are marked on the left side of the plot. Those of $d(2L^*_{\mathrm{2D}}/2L_{\mathrm{3D}})/d(\log_2 \nu^2)$, and $d(2t^*/2L_{\mathrm{3D}})/d(\log_2 \nu^2)$ are marked on the right side.

will approach a constant that is independent of system size, with increasing ν^2. In this case, N_c/ν^2, and M/ν^2 will be decreasing functions of ν^2. On the other hand, if N_c/ν^2 and M/ν^2 scales with or increases with system size, ν^2, it indicates that $N_c, M \to \nu^2$ as $\nu^2 \to \infty$. This points to a tough fracture mode (Kachhwah and Mahesh 2020).

Similarly, $\lim_{\nu^2 \to \infty} 2L^*_{\mathrm{2D}}/2L_{\mathrm{3D}}$ determines the longitudinal extent of the weakest-link in a physical composite. A longitudinally localised weakest-link is indicated only if $2L^*_{\mathrm{2D}}/2L_{\mathrm{3D}}$ decreases, or approaches a constant with increasing ν^2. In this case, the fracture surface will be transverse and smooth. However, if $2L^*_{\mathrm{2D}}/2L_{\mathrm{3D}}$ increases with increasing ν^2, the weakest-link becomes delocalised longitudinally. In this case, the fracture surface will be step, broom or brush-like (Hull and Clyne 1996).

Figs. 12a, and 12b show the variation of N_c/ν^2, and M/ν^2 with ν^2 for $\rho = 10$ composites. Similarly, Figs. 12c and 12d show the variation of the fractional length of the weakest-link, $2L^*_{2\mathrm{D}}/2L_{3\mathrm{D}}$, and the effective fractional debond length, $2t^*/2L_{3\mathrm{D}}$ with ν^2. Straight lines, obtained by fitting the points using linear least squares are also drawn. These lines are drawn with solid lines if they have a negative slope, and with dashed lines if they have a positive slope. The variation with τ_0/σ_0 of the slopes, $d(\log_2 M/\nu^2)/d(\log_2 \nu^2)$, and $d(\log_2 N_c/\nu^2)/d(\log_2 \nu^2)$ of the straight lines in Figs. 12a, and 12b is shown as solid lines in Fig. 13. The slopes of the lines fitting Figs. 12c and 12d, which represent $d(2t^*/2L_{3\mathrm{D}})/d(\log_2 \nu^2)$, and $d(2L^*_{2\mathrm{D}}/2L_{3\mathrm{D}})/d(\log_2 \nu^2)$, respectively, are shown as dashed lines.

It is seen in Figs. 12a, 12b that for $\tau_0/\sigma_0 \geq 0.4$, both N_c/ν^2, and M/ν^2, decrease with increasing ν^2. This points to the brittle fracture mode. However, for $\tau_0/\sigma_0 \leq 0.3$, both N_c/ν^2, and M/ν^2 increase with ν^2, indicating the tough mode of fracture. Thus the tough brittle transition for $\rho = 10$ composites can be constrained to $0.3 \leq \tau_0/\sigma_0 \leq 0.4$. The tough-brittle transition reveals itself as a change of sign of $d(\log_2 N_c/\nu^2)/d(\log_2 \nu^2)$, and $d(\log_2 M/\nu^2)/d(\log_2 \nu^2)$ in Fig. 13. In Figs. 12c and 12d, $2L^*_{2\mathrm{D}}/2L_{3\mathrm{D}}$, and $2t^*/2L_{3\mathrm{D}}$, are seen to slightly decrease with increasing ν^2 only for $\tau_0/\sigma_0 \geq 0.7$. In Fig. 13, it is seen that $d(2L^*_{2\mathrm{D}}/2L_{3\mathrm{D}})/d(\log_2 \nu^2) \leq 0$ for $\tau_0/\sigma_0 \geq 0.7$. This indicates a longitudinally localised weakest-link, which will produce smooth transverse fracture surfaces.

In the regime $\tau_0/\sigma_0 \leq 0.5$, both $2L^*_{2\mathrm{D}}/2L_{3\mathrm{D}}$, and $2t^*/2L_{3\mathrm{D}}$, are seen to increase with ν^2. This indicates that the weakest-link failure event extends longitudinally with increasing ν^2, producing a broom-like or brush-like fracture surface (Hull and Clyne 1996). At two points in this parameter regime, $\tau_0/\sigma_0 \in \{0.4, 0.5\}$, the brittle fracture mode prevails, i.e., the weakest-link failure event is localised in the transverse direction. Nevertheless, the weakest-link event is found to be longitudinally delocalised. This suggests that longitudinal and transverse localisation of the weakest-link failure event are governed by distinct phenomena.

As seen in Fig. 13, both $d(2L^*_{2D}/2L_{3D})/d(\log_2 \nu^2)$, and $d(2t^*/2L_{3D})/d(\log_2 \nu^2)$ are maximal in the tough regime, $\tau_0/\sigma_0 \leq 0.3$. In this regime, the weakest-link failure event is localised neither longitudinally, nor transversely. Physically, a brush-like fracture surface with extensive fibre pull-out will be realised.

The dependence of the tough-brittle transitional τ_0/σ_0 on fibre strength variability, quantified by ρ is next examined. The foregoing simulations, and computations are repeated for the case of $(\rho, 2L_{3D}) = (20, 5)$ model composites. The scaling of N_c/ν^2, and M/ν^2 with ν^2 so obtained is shown in Fig. 14, for $\tau_0/\sigma_0 \in \{0.1, 0.3, 0.5\}$. It is seen that according to both the Curtin (1998), and tight cluster growth models, the fracture mode remains brittle over this range. The tough-brittle transition thus occurs at $\tau_0/\sigma_0 < 0.1$ for $\rho = 20$ composites. This indicates that the tough-brittle transitional τ_0/σ_0 decreases with increasing ρ, i.e., with decreasing fibre strength variability.

In the foregoing analysis, it has been tacitly assumed that the trends observed over the composite size range, $\nu^2 \in \{2^8, 2^{10}, 2^{12}\}$ can be extrapolated to much larger sizes. It is infeasible to test the validity of this assumption computationally, at present. This is a limitation of the present study.

4.6 Fracture development in the tough and brittle regimes

Fracture development in the model composites proceeds through a complex succession of fibre breaks, and matrix failures. In the fracture simulation algorithm described in Sec. 2.1, the average load per fibre, $\langle\sigma\rangle$, is incremented monotonically. At the last increment, $\langle\sigma\rangle =$

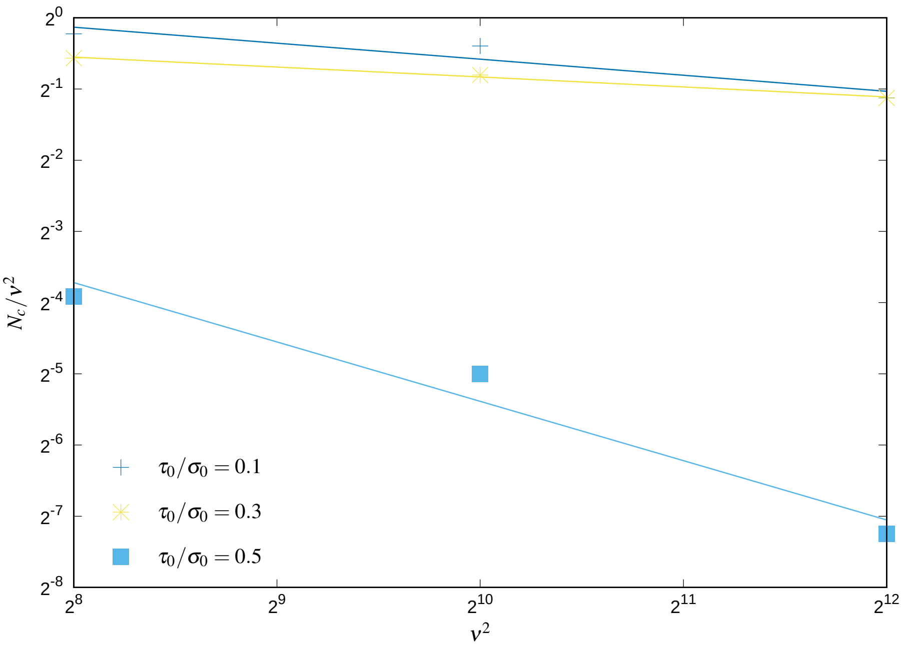

(a)

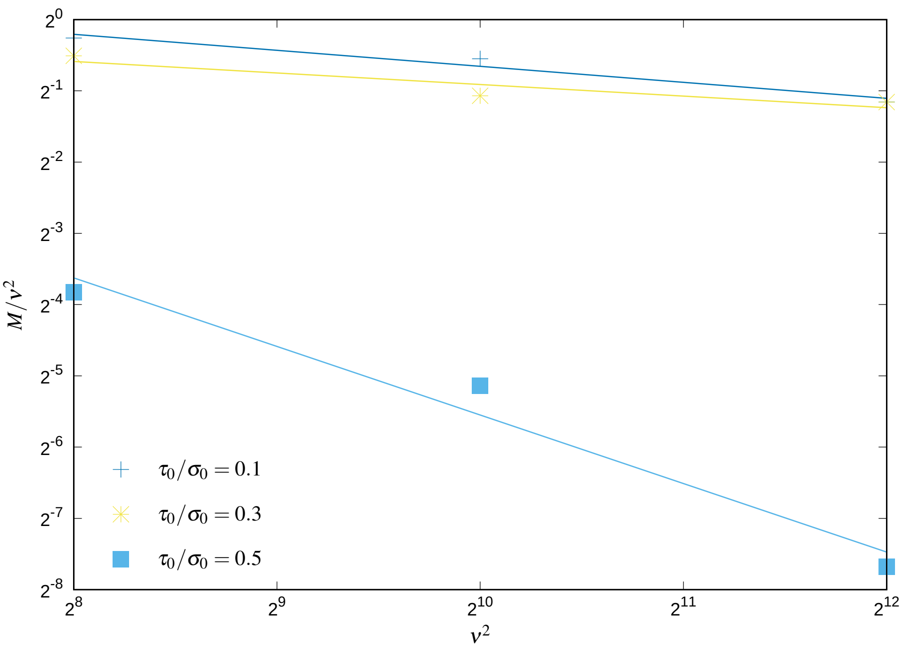

(b)

Fig. 14: Scaling of the fractional transverse size (a) N_c/ν^2, and (b) M/ν^2, in $\rho = 20$, $2L_{3D} = 5$, 3D composites with the number of fibres, ν^2. Lines represent linear least squares fits of the points.

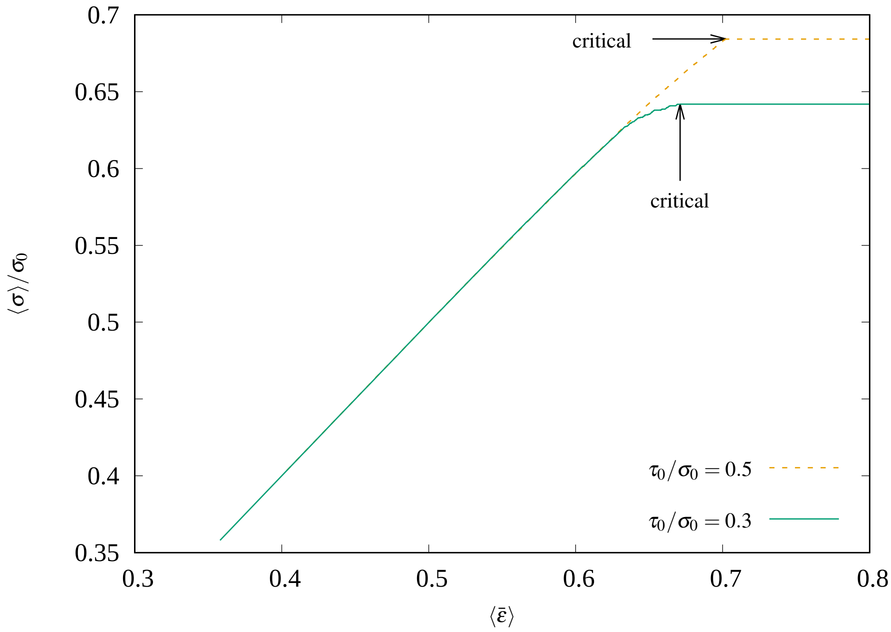

Fig. 15: Normalised average stress-average strain curves of the median $(v^2, \rho, 2L_{3D}) = (2^{12}, 10, 5)$ specimen on either side of the tough-brittle transition.

$\langle\sigma\rangle^{\text{ult}}$. The configuration of fibre breaks and matrix failures just prior to the last increment of the applied stress is termed the critical configuration. Thus, an infinitesimal increment in the stress applied to the critical configuration will create a running catastrophic crack that causes specimen fracture.

Corresponding to the $N_{\text{sim,3D}} = 256$ statistically identical model specimens simulated for each $(v^2, \rho, 2L_{3D}, \tau_0/\sigma_0)$, there are two median specimens. Fig. 15 shows the normalised average stress-strain curve obtained for the weaker of the two median $(v^2, \rho, 2L_{3D}) = (2^{12}, 10, 5)$ specimen. Curves for $\tau_0/\sigma_0 = 0.3$ in the tough regime, and for $\tau_0/\sigma_0 = 0.5$ in the brittle regime are plotted. The critical load is marked in each case. It is seen that in the brittle specimen, the stress-strain curve remains nearly straight until the critical load, while in the ductile specimen the stress-strain graph curves substantially before the critical load is reached.

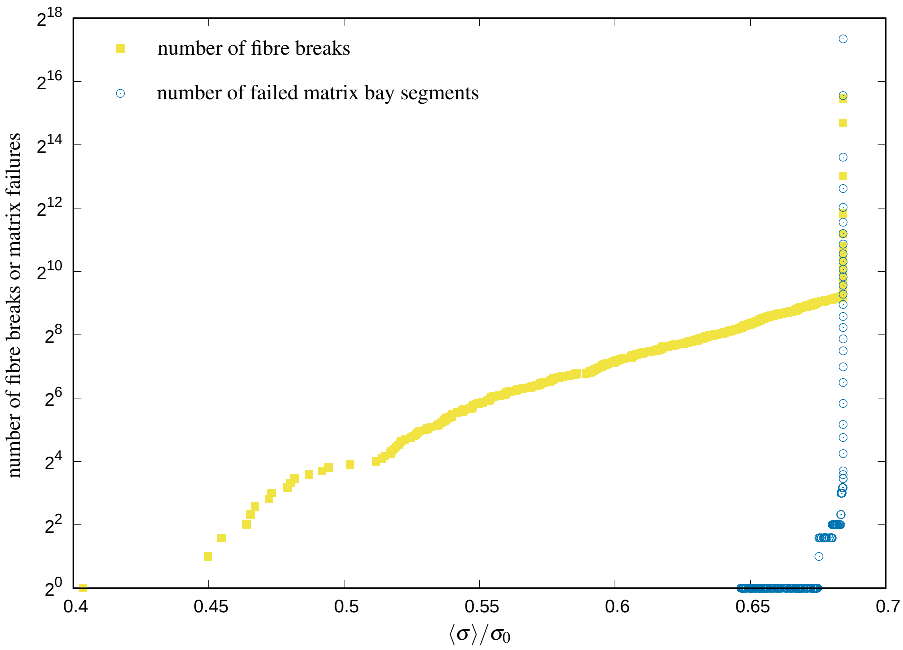

(a) $\tau_0/\sigma_0 = 0.5$, $\rho = 10$, $v^2 = 2^{12}$

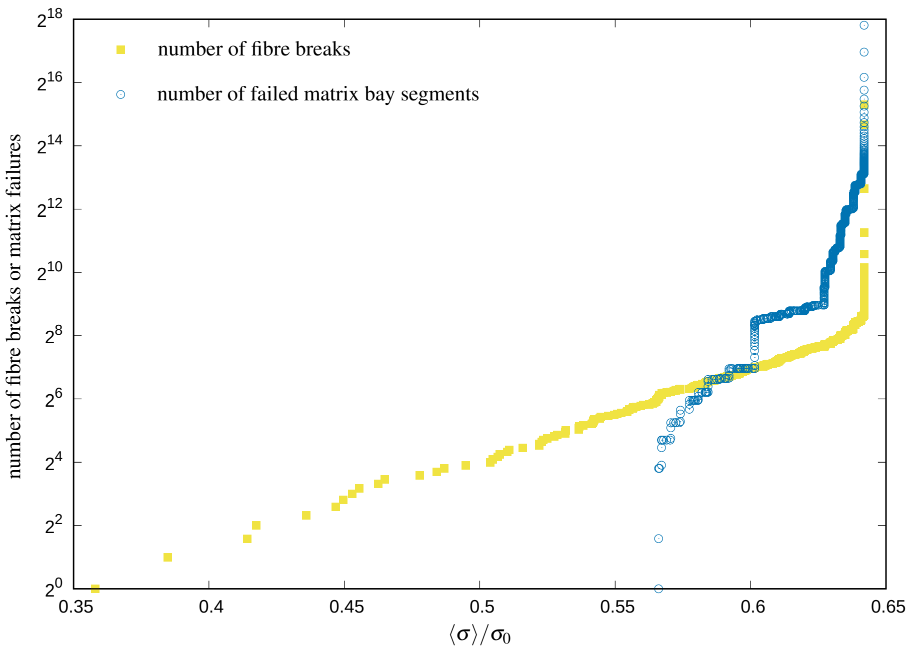

(b) $\tau_0/\sigma_0 = 0.3$, $\rho = 10$, $v^2 = 2^{12}$

Fig. 16: Accumulation of fibre breaks and matrix failures with applied stress in the weaker median $(v^2, \rho, 2L_{3D}) = (2^{12}, 10, 5)$ specimen with (a) $\tau_0/\sigma_0 = 0.5$ (brittle regime), and (b) $\tau_0/\sigma_0 = 0.3$ (tough regime).

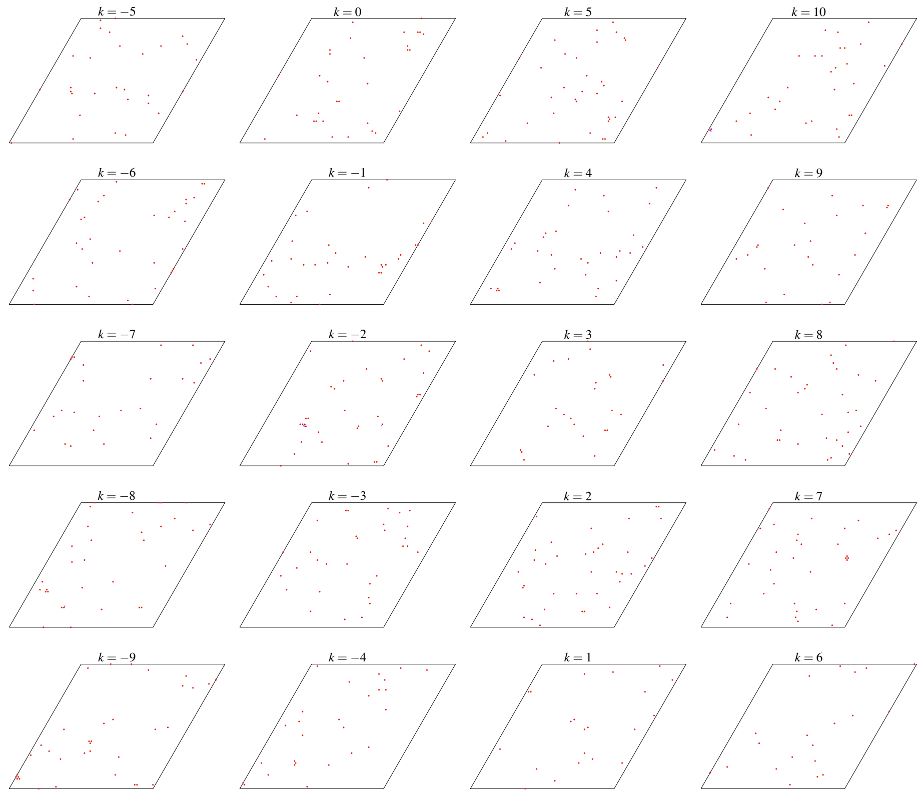

Fig. 17: Critical configuration of the weaker median $\rho = 10$, $\nu^2 = 2^{12}$ specimen, with $\tau_0/\sigma_0 = 0.5$. Fibre breaks are depicted by red dots, and failed matrix bays by blue lines. Only eight matrix bays are failed. They are in the $k \in \{-8,-7,-2,10\}$ blocks.

Figs. 16a, and 16b show the accumulation of fibre breaks and matrix failures with applied stress, $\langle\sigma\rangle/\sigma_0$, in the weaker median $(\nu^2, \rho, 2L_{3D}) = (2^{12}, 10, 5)$ brittle and tough specimen with $\tau_0/\sigma_0 = 0.5$, and 0.3, respectively. The ordinate scale in these plots is logarithmic.

In both the brittle (Fig. 16a) and tough specimens (Fig. 16b), the accumulated number of fibre breaks scales approximately exponentially up to the critical configuration, with applied stress, $\langle\sigma\rangle$. The number of fibre breaks in the critical configuration is only slightly larger

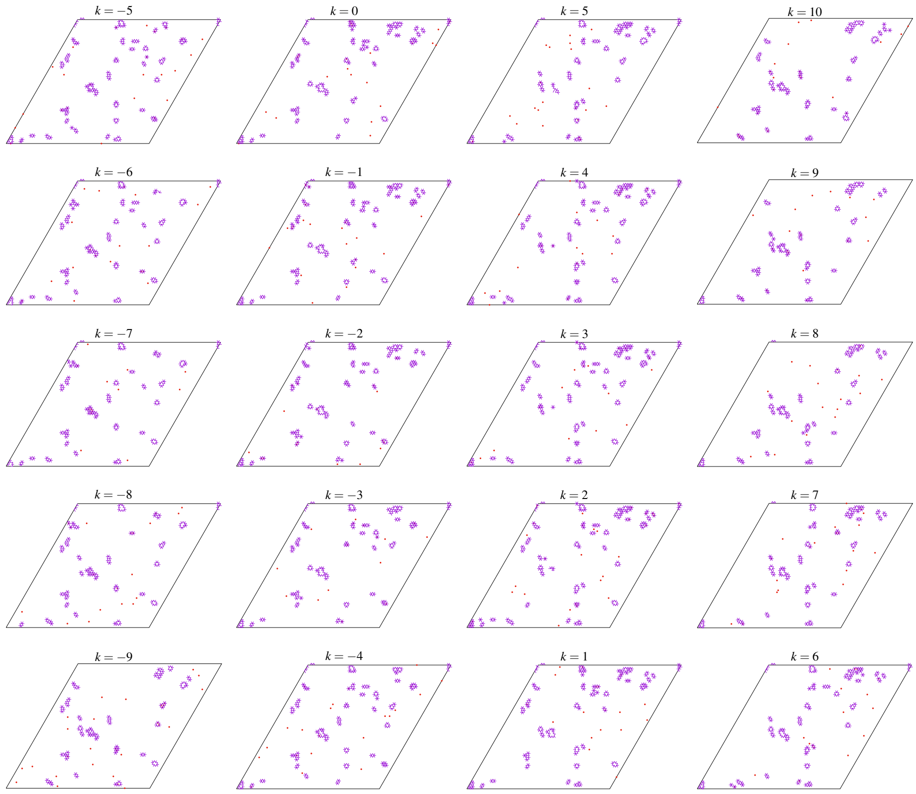

Fig. 18: Critical configuration of the weaker median $\rho = 10$, $v^2 = 2^{12}$ tough specimen, with $\tau_0/\sigma_0 = 0.3$. Fibre breaks are depicted by red dots, and failed matrix bays by blue lines.

in the brittle specimen of Fig. 16a than that in the tough specimen of Fig. 16b. The key difference between the tough and brittle specimens is the number of matrix failures: Very few matrix segments are failed at the critical configuration in the brittle specimen, as seen in Fig. 16a. However, profuse matrix failure, which outstrips the rate of fibre breakage, occurs just before the critical configuration is reached in the tough specimen, as shown in Fig. 16b. This points to a central role for matrix failure in the transition from the brittle mode to the tough mode.

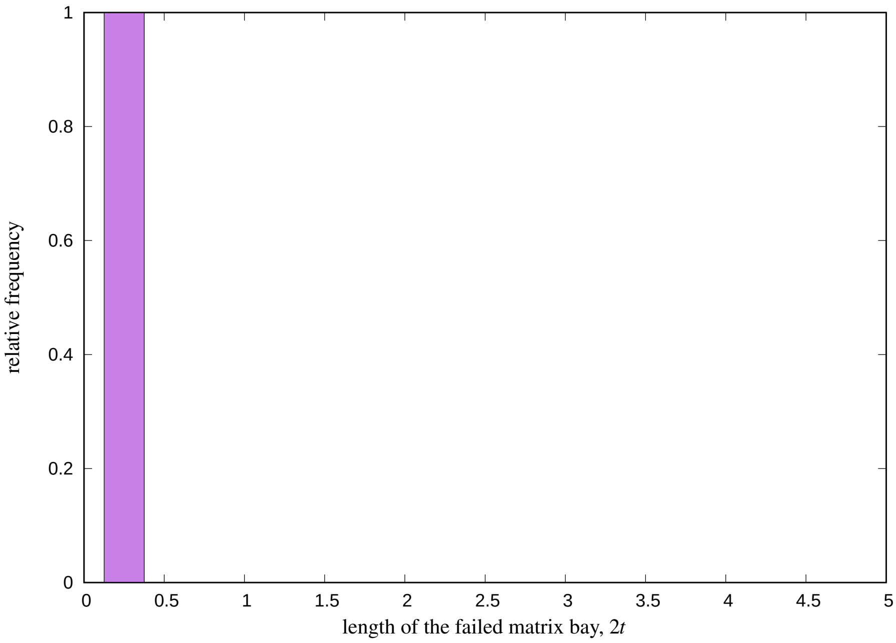

(a) $\tau_0/\sigma_0 = 0.5$

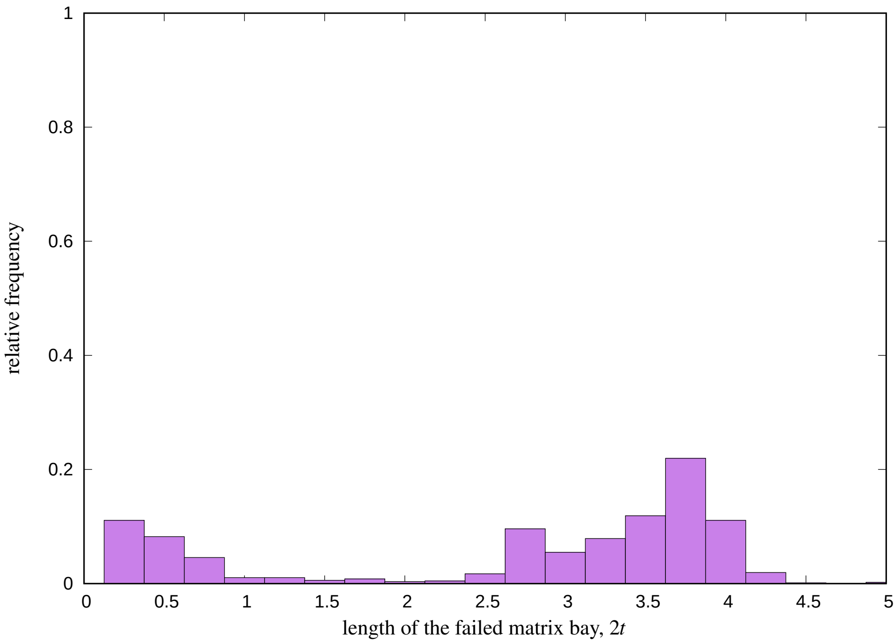

(b) $\tau_0/\sigma_0 = 0.3$

Fig. 19: Histograms of the length of matrix failures at the critical configuration for the weaker median $(v^2, \rho, 2L_{\text{3D}}) = (2^{12}, 10, 5)$ specimen with (a) $\tau_0/\sigma_0 = 0.5$ (brittle regime), and (a) $\tau_0/\sigma_0 = 0.3$ (tough regime).

In experimental studies of composite fracture on both sides of the tough-brittle transition, Dzenis and Qian (2001), Sket et al (2012), and Scott et al (2011) have noted that most failure events occur just prior to composite fracture. The present observation of exponential scaling of fibre breakage, and matrix failure events is consistent with these experimental observations.

Figs. 17, and 18 show the fibre breaks, and matrix failures in the critical configurations of the weaker median $(\nu^2, \rho, 2L_{3\mathrm{D}}, \tau_0/\sigma_0) = (2^{12}, 10, 5, 0.5)$ (brittle), and $(\nu^2, \rho, 2L_{3\mathrm{D}}, \tau_0/\sigma_0) = (2^{12}, 10, 5, 0.3)$ (tough), specimen, respectively. Fibre breaks at each of the $2K = 20$ block boundaries are indicated by red dots. Failed matrix segments in the k-th block, for $k \in \{-K+1, -K+2, \ldots, K\}$, are depicted by a blue line segment. In both Figs. 17, and 18, the fibre breaks at the critical configuration are dispersed throughout the model composite. Very few clusters of fibre breaks are seen. In computed tomographic studies of composite damage, Sket et al (2012) and Scott et al (2011), also noted the absence of large clusters of breaks. The present observations are consistent with the experimental ones.

Only eight failed matrix bay segments are seen in the brittle specimen of Fig. 17. These matrix failures link fibre breaks in neighbouring fibres in adjacent blocks. However, in the tough specimen of Fig. 17, a number of matrix bays are failed. Matrix failures are seen to issue from fibre breaks, and extend several blocks in the longitudinal direction.

Fig. 19 shows histograms of the length of matrix failures at the critical configuration for the two median specimen. Fig. 19a shows that in the brittle specimen with $\tau_0/\sigma_0 = 0.5$, every matrix failure is of length Δ. These matrix failures typically link up fibre breaks in neighbouring fibres Δ apart in the longitudinal direction. On the other hand, as seen in Fig. 19b, in the tough specimen with $\tau_0/\sigma_0 = 0.3$, a number of long matrix failures of length $2t \gg \Delta$ are seen to develop.

It is concluded from Figs. 17, 18, and 19 that while in the brittle regime, matrix failures only connect fibre breaks in adjacent block boundaries, in the tough regime, matrix bay failures originate at fibre breaks, and propagate extensively in the longitudinal direction.

4.7 Mechanistic cause of the fracture mode transition

Section 4.6 shows that fracture development in the tough regime is qualitatively different from that in the brittle regime. The tough regime is characterised by long matrix tears, which are nearly absent in the brittle regime. Presently, the mechanistic cause for this difference is identified by examining the stress redistribution from a single broken fibre, and from clusters of fibre breaks, with failed abutting matrix bays. Attention is particularly focused on the effect of long failed matrix bays.

First, the maximum stress overload due to a single fibre break surrounded by matrix failures in all the abutting matrix bays is considered. Let the fibre break be located at $(m,n,\zeta) = (0,0,0)$, and let the matrix bays abutting the broken fibre be failed up to $\zeta = \pm t$. Maximum stress concentration is realised at $(m,n,\zeta) = (1,0,0)$. Following the notation of Sec. 2.1, the stress overload is denoted $\tilde{\sigma}_{10}(\zeta = 0)$. The inset of Fig. 20 shows the fibre break, and matrix failures schematically.

Fig. 20 shows the variation of $\tilde{\sigma}_{10}(\zeta = 0)$, with debond half-length, t in $\nu^2 = 2^8$, and 2^{12} model 3D composites of length $2L_{3\mathrm{D}} = 5$. For $t \ll 2L_{3\mathrm{D}}$, the variation is seen to be exponential: $\tilde{\sigma}_{m0} \sim \exp(-t/50)$. The exponential decrease of $\tilde{\sigma}_{10}(t)$ with increasing t implies that matrix failure severely delocalises stress overloads near fibre breaks, and thereby inhibits the brittle fracture mode.

As the debond length $2t$ approaches the length of the simulation cell, $2L_{3\mathrm{D}} = 5$, the variation deviates from exponential dependence. This can be understood by noting that in

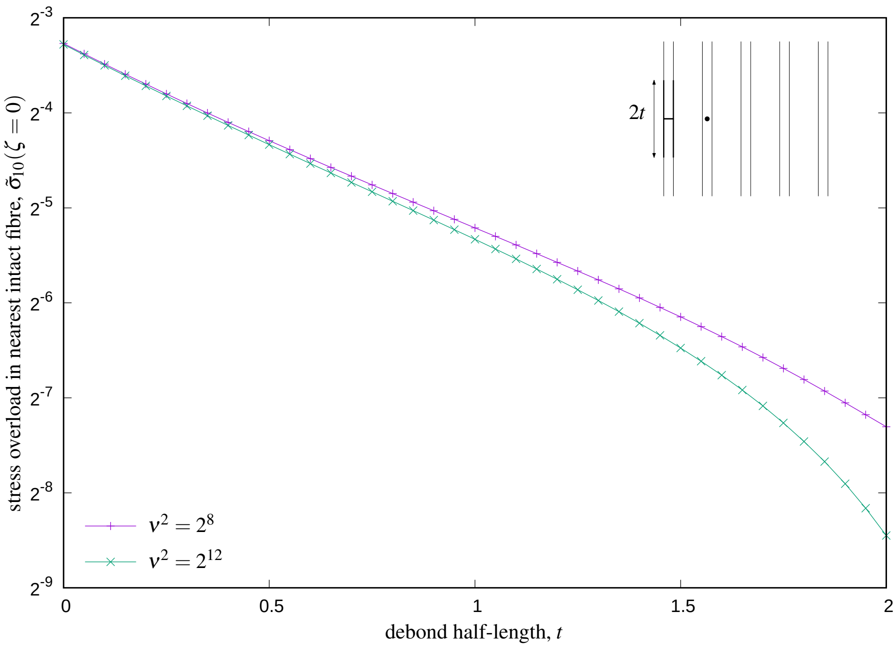

Fig. 20: Stress overload in the nearest neighbour of a single break flanked by debonds of variable length. The fibre break is located at $m = n = \zeta = 0$. $2L_{3D} = 5$.

the limit of $t \to L_{2D}$, $\tilde{\sigma}_{10}$ must approach the overload given by equal load sharing Eq. (31). The deviation from exponential decay is thus an artefact of finite fibrewise length of the model composite.

In order to understand the growth of matrix failures around clusters of fibre breaks, the shear stresses induced in the matrix are next considered. Fig. 21 plots the variation of the maximum shear stress, $\max \tau_{mnik}$, developed in $(\nu^2, 2L_{3D}) = (2^{12}, 5)$ model composites with penny-shaped clusters of fibre breaks located in the $\zeta = 0$ plane, and matrix failures extending over $\zeta \in (-t, t)$ in all the matrix bays between all intact fibres and broken fibres. Matrix failures are thus confined to the edge of the penny-shaped clusters, as shown in the inset of Fig. 21. The maximum shear stress, $\max \tau_{mnik}$, develops at the tip of the failed

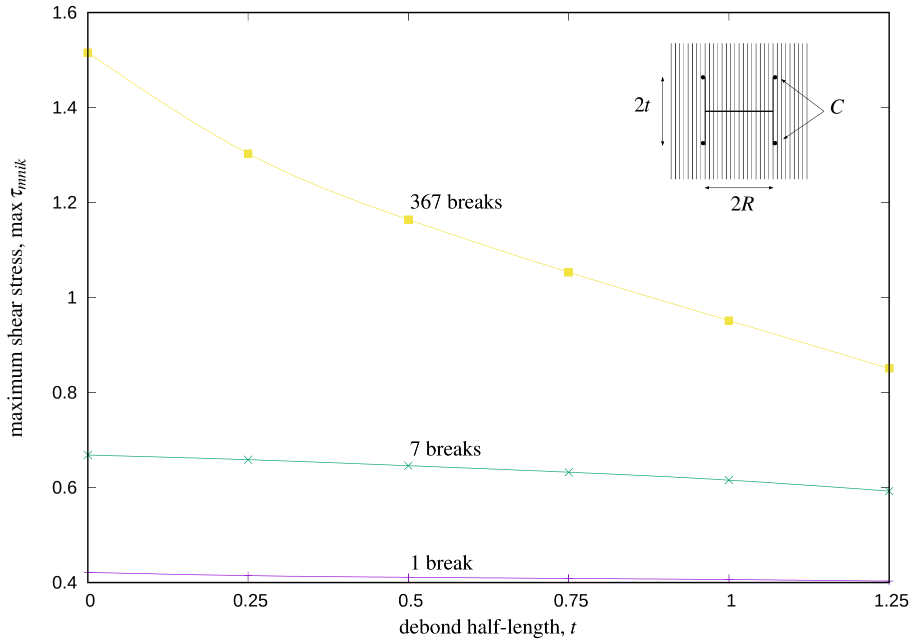

Fig. 21: Variation of the maximum shear stress, max τ_{mnik}, developed in the matrix bays with debond length, $2t$, induced by penny-shaped transverse clusters comprised of 1, 7, and 367 fibre breaks. The normalised radii, R of these clusters are 0, 1, and 10, respectively. $\nu^2 = 2^{12}$, and $2L_{3D} = 5$.

interface, labelled C in the inset. It decreases monotonically with increasing t. However, the rate of decrease depends on the size of the cluster of breaks. For a single fibre break, max τ_{mnik} decreases only about 4% as t increases from $t = 0$, to $t = 1.25$. This suggests that matrix failure, once initiated round a single break will readily propagate in the fibrewise direction, with only a slight increment in the applied stress, $\langle\sigma\rangle$.

For larger clusters, however, max τ_{mnik} decreases more with t. For example, for the penny-shaped clusters comprised of 7, and 367 breaks, τ_{mnik} decreases by 11%, and 44%, respectively from $t = 0$ to $t = 1.25$. Thus, matrix failures initiated around larger clusters propagate less readily in the fibrewise direction than those around smaller clusters.

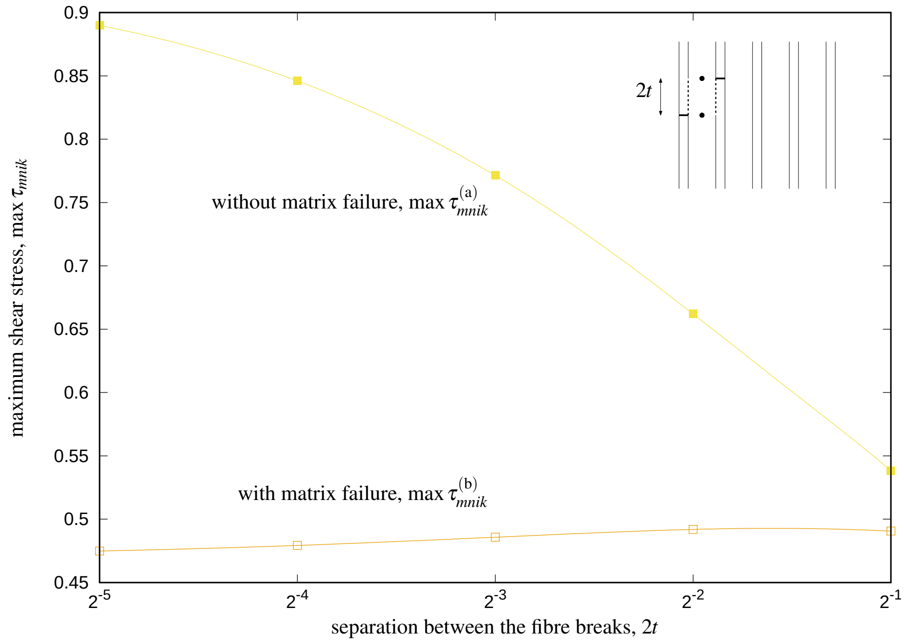

Fig. 22: Variation of the maximum shear stress, $\tau_{mni}(C)$, developed in the matrix bay between a pair of breaks in neighbouring fibres, located $2t$ apart in the fibrewise direction. max $\tau^{(a)}_{mnik}$ and max $\tau^{(b)}_{mnik}$ represent the maximum shear stress developed in the matrix when (a) all the matrix bays are intact, and (b) with the intervening matrix bay failed.

It is recalled that the critical configuration of the tough specimen shown in Fig. 18 contained numerous long matrix failures around small clusters of breaks. According to Fig. 21, these are the matrix failures that will propagate most readily. Once propagated, the matrix failures, will reduce the stress overload on neighbouring fibres exponentially, according to Fig. 20. Thus, the mechanistic cause for the transition to the tough mode from the brittle mode is identified as the formation of matrix failures, around single fibre breaks, or small clusters of breaks, and their longitudinal propagation.

In the brittle regime, matrix failure does not accompany single fibre breaks, as seen in Fig. 17. However, a few matrix bay segments of length Δ fail. To understand their origin, the maximum shear stress induced by two fibre breaks in neighbouring fibres, vertically staggered by distance $2t$ is now considered. Two cases are considered: (a) where all the matrix bays in the model are intact, and (b) where the single matrix bay between the two breaks is failed. The two cases are schematically shown in the inset of Fig. 22.

Fig. 22 shows that as the breaks approach each other, the maximum shear stress $\max \tau_{mnik}^{(a)}$ that develops in the intervening intact matrix bay increases. If the intervening matrix bay between the two breaks fails, the shear stress in the failed bay becomes zero, and the maximum shear stress $\max \tau_{mnik}^{(b)}$, is realised in the other matrix bays abutting the fibre breaks. It is seen that $\max \tau_{mnik}^{(b)}$ is nearly independent of the longitudinal spacing $2t$ between the breaks. Also for small $2t$, $\max \tau_{mnik}^{(b)}$ is significantly smaller than $\max \tau_{mnik}^{(a)}$. Matrix bay failure between breaks in neighbouring fibres thus relieves the shear stress in the matrix. This mechanism is responsible for the small number of short matrix failures in the brittle mode.

In summary, the tough fracture mode is realised if the interfacial strength, τ_0/σ_0, is small enough that matrix failure occurs in the matrix bay segments abutting single breaks, or small clusters of breaks. Such matrix failures propagate readily in the fibrewise direction. However, if the interface is strong enough to suppress the failure of matrix bay segments around single breaks, or small clusters of breaks, the brittle fracture mode results. The occurrence of short matrix bay failures between staggered fibre breaks for stress relief in the matrix does not affect the brittle mode.

He et al (1993) and Curtin (1993) have proposed mechanisms underlying the tough-brittle transition in ceramic matrix composites with frictionally sliding interfaces. He et al (1993) have shown that load transfer from a broken fibre to its neighbours varies continuously with the frictional strength of the interface. They have proposed that the fracture mode will be tough if the probability of survival of the nearest neighbours of a broken fibre exceeds that of more distant neighbours.

In the present model polymer matrix composites, load sharing from a broken fibre to its neighbours varies discontinuously across the tough-brittle transition. On the brittle side, the absence of long failed matrix bays produces localised load sharing, while on the tough side, their presence severely delocalises the load sharing. The transition in the present model arises from discontinuity in the load sharing at the transitional τ_0/σ_0. It is thus a stronger transition than that in the model of He et al (1993).

Curtin (1993) proposed that composite failure occurs by the failure of the weakest spherical region within it following global load sharing. He took its radius to be the length over which load is recovered in a broken fibre through frictional sliding. With decreasing interfacial strength, enlargement of the spherical region results in a crossover from the brittle to tough fracture modes. This ansatz results in a smooth cross-over from the tough to brittle mode.

In the present model composite, the fracture mode is found to localise differently in the longitudinal and transverse directions, as noted in Sec. 4.5. Also, the model exhibits a sharp transition in the transverse direction.

4.8 Limitations

Computational limitations associated with small simulation cell sizes, and coarse fibre wise discretisation have been noted previously in Sec. 4.2, and 4.5. Other limitations of the present study are now enumerated.

First, the assumption that interface failure occurs only due to shear stresses is admittedly simplistic. Cook and Gordon (1964) showed that interfacial debonding is also determined by normal stresses transverse to the fibre direction. In principle, it is possible to account for transverse normal stresses using the shear-lag model of Goree and Gross (1980). However, this will double the size of the already computationally intensive stress analysis problem. Second, the assumption that a debonded interface transmits no shear may be unreasonable if large transverse compressive stresses are locked into the matrix when the composite is cooled from the curing temperature. In this case, the frictional stresses across the interface may be considerable. Again, it seems possible to extend the present shear-lag model to account for this, albeit at greater computational cost. Third, the interfacial strength has been assumed deterministic. Ma et al (2017) have reported variability in the interfacial strength itself, which introduces variability into the nature of the fracture surface itself. Fourth, the transitional value of the ratio of the interfacial strength to the fibre strength has only been evaluated for the case of Weibull exponent 10, which represents relatively low fibre strength variability. Attempts to capture the transitional value for Weibull exponent 5 have not been successful, since the size of the 2D weakest link exceeds the presently feasible largest simulation cell comprised of 2^{12} fibres. Fifth, fracture simulations must necessarily be performed on finite sized simulation cells. The periodic images will therefore necessarily influence the estimated characteristic sizes of the weakest-link failure event. Even if fracture could be simulated in much larger periodic cells than the present ones, the simulations based approach can at best only bound the transitional value (Nishimori and Ortiz 2010; Binder 2003), and not obtain it exactly. Fifth, fracture mechanisms not accounted for presently have been observed experimentally. For example, Sket et al (2012) and Scott et al (2011) observed fibre splitting, and matrix splitting in glass- and carbon-epoxy laminates, respectively, through in-situ computed tomography studies, while Dzenis and Qian (2001) observed extensive matrix splitting through acoustic emission, and direct observations.

5 Conclusion

With decreasing interfacial strength, a tough-brittle transition occurs in model polymer matrix composites. The interfacial strength at which the transition occurs depends on the fibre strength variability. In the brittle regime, the developing transverse crack becomes catastrophic before long interfacial failures can form at its front. In the tough regime, long interfacial failures form even around single fibre breaks, or small clusters of fibre breaks. These delocalise the stress overloads dramatically, and cause global fracture development.

References

Banholzer B, Brameshuber W (2001) Eine methode zur beschreibung des verbundes zwischen faser und zementgebundener matrix. Beton Stahlbetonbau 96(10):663–669

Beyerlein IJ, Phoenix SL (1997) Statistics of fracture for an elastic notched composite lamina containing Weibull fibers I. Features from Monte-Carlo simulation. Eng Fract Mech 57(2-3):241–265

Binder K (2003) Overcoming the limitation of finite size in simulations: From the phase transition of the Ising model to polymers, spin glasses, etc. In: AIP Conference Proceedings, American Institute of Physics, vol 690, pp 74–84

Cook J, Gordon J (1964) A mechanism for the control of crack propagation in all-brittle systems. Proc R Soc Lond A 282(1391):508–520

Curtin W (1993) The tough to brittle transition in brittle matrix composites. J Mech Phys Solids 41(2):217–245

Curtin W (1998) Size scaling of strength in heterogeneous materials. Phys Rev Lett 80(7):1445

Curtin W (2000) Dimensionality and size effects on the strength of fiber-reinforced composites. Compos Sci Tech 60(4):543–551

Daniels HE (1945) The statistical theory of the strength of bundles of threads. Proc R Soc London A 183(995):405–435

Dzenis YA, Qian J (2001) Analysis of microdamage evolution histories in composites. International journal of solids and structures 38(10-13):1831–1854

Epstein B (1948) Statistical aspects of fracture problems. J Appl Phys 19(2):140–147

Goree JG, Gross RS (1980) Analysis of a unidirectional composite containing broken fibers and matrix damage. Eng Fract Mech 13(3):563–578

Gücer D, Gurland J (1962) Comparison of the statistics of two fracture modes. J Mech Phys Solids 10(4):365–373

Gupta A, Mahesh S, Keralavarma SM (2017) Strength distribution of large unidirectional composite patches with realistic load sharing. Phys Rev E 96(4):043,002

Gupta A, Mahesh S, Keralavarma SM (2018) A fast algorithm for the elastic fields due to interacting fibre breaks in a periodic fibre composite. International Journal of Fracture 211(1-2):295–303

Habeeb CI, Mahesh S (2015) Strength distribution of planar local load-sharing bundles. Physical Review E 92(2):022,125

Hansen A, Hemmer P, Pradhan S (2015) The Fiber Bundle Model: Modeling Failure in Materials. Statistical Physics of Fracture and Breakdown, Wiley

Harlow DG, Phoenix S (1981a) Probability distributions for the strength of composite materials I: two-level bounds. Int J Fracture 17(4):347–372

Harlow DG, Phoenix SL (1981b) Probability distributions for the strength of composite materials II: A convergent sequence of tight bounds. Int J Fracture 17(6):601–630

He M, Evans AG, Curtin WA (1993) The ultimate tensile strength of metal and ceramic-matrix composites. Acta metall mater 41(3):871–878

Hedgepeth JM (1961) Stress concentrations in filamentary structures. Tech. Rep. RN D-882, NASA

Hedgepeth JM, Van Dyke P (1967) Local stress concentrations in imperfect filamentary composite materials. J Compos Mater 1(3):294–309

Herrera-Franco P, Drzal L (1992) Comparison of methods for the measurement of fibre/matrix adhesion in composites. Compos A 23(1):2–27

Hull D, Clyne TW (1996) An introduction to composite materials. Cambridge university press

Ibnabdeljalil M, Curtin W (1997a) Strength and reliability of fiber-reinforced composites: localized load-sharing and associated size effects. Int J Solids Struct 34(21):2649–2668

Ibnabdeljalil M, Curtin W (1997b) Strength and reliability of notched fiber-reinforced composites. Acta mater 45(9):3641–3652

Kachhwah US, Mahesh S (2020) Tough-brittle transition in the planar fracture of unidirectional fiber composites. Physical Review E 101(6):063,002

Karger-Kocsis J, Mahmood H, Pegoretti A (2015) Recent advances in fiber/matrix interphase engineering for polymer composites. Prog Mater Sci 73:1–43

Kumar MS, Raghavendra K, Venkataswamy MA, Ramachandra HV (2012) Fractographic analysis of tensile failures of aerospace grade composites. Mater Res 15(6):990–997

Landis CM, Beyerlein IJ, McMeeking RM (2000) Micromechanical simulation of the failure of fiber reinforced composites. Journal of the Mechanics and Physics of Solids 48(3):621–648

Ma Y, Yang Y, Sugahara T, Hamada H (2016) A study on the failure behavior and mechanical properties of unidirectional fiber reinforced thermosetting and thermoplastic composites. Compos B 99:162–172

Ma Y, Ueda M, Yokozeki T, Sugahara T, Yang Y, Hamada H (2017) A comparative study of the mechanical properties and failure behavior of carbon fiber/epoxy and carbon fiber/polyamide 6 unidirectional composites. Compos Struct 160:89–99

Mahesh S (2020) A fast algorithm for fracture simulations representing fibre breakage and matrix failure in three-dimensional fibre composites. Int J Fracture 222(1):75–109

Mahesh S, Phoenix SL, Beyerlein IJ (2002) Strength distributions and size effects for 2D and 3D composites with Weibull fibers in an elastic matrix. Int J Fracture 115(1):41–85

Mahesh S, Gupta A, Kachhwah US, Sheikh N (2019) A fast algorithm to simulate the failure of a periodic elastic fibre composite. Int J Fracture 217(1):127–135

McCartney L, Smith R (1983) Statistical theory of the strength of fiber bundles. J Appl Mech 50(3):601–608

Nishimori H, Ortiz G (2010) Elements of phase transitions and critical phenomena. OUP Oxford

Robinson P, Greenhalgh E, Pinho S (2012) Failure mechanisms in polymer matrix composites: Criteria, testing and industrial applications. Elsevier

Scott A, Mavrogordato M, Wright P, Sinclair I, Spearing S (2011) In situ fibre fracture measurement in carbon–epoxy laminates using high resolution computed tomography. Compos Sci Tech 71(12):1471–1477

Sket F, Seltzer R, Molina-Aldareguía J, Gonzalez C, LLorca J (2012) Determination of damage micromechanisms and fracture resistance of glass fiber/epoxy cross-ply laminate by means of x-ray computed microtomography. Compos Sci Tech 72(2):350–359

Smith R (1980) A probability model for fibrous composites with local load sharing. Proc R Soc London A 372(1751):539–553

Smith R, Phoenix S, Greenfield M, Henstenburg R, Pitt R (1983) Lower-tail approximations for the probability of failure of three-dimensional fibrous composites with hexagonal geometry. Proc R Soc London A 388(1795):353–391

Weibull W (1952) A statistical distribution function of wide applicability. J Appl Mech 19(2):233–234

Zhandarov S, Mäder E (2005) Characterization of fiber/matrix interface strength: applicability of different tests, approaches and parameters. Compos Sci Tech 65(1):149–160